AN ABSTRACT OF THE THESIS OF

Sara K. Culley for the degree of Master of Science in Oceanography presented on March 21, 1986.

Title: Standing Edge Waves on a Pocket Beach

Abstract approved: Redacted for privacy
Robert A. Holman

An experiment was designed to measure infragravity edge waves, taking advantage of the natural resonance restrictions created by topographic trapping of standing waves on a beach bounded by reflective headlands. On four different days under varying incident conditions, concurrent time series of wave runup at many transects alongshore were generated from time-lapse films of the swash zone. Spectral analyses of the data showed strong dominance of the infragravity-band (.003Hz-.05Hz) on 3 of the 4 days when at least 95% of the runup variance was below .05Hz. Interesting spectral patterns at frequencies near .01Hz, with energy varying between peaks and valleys alongshore, suggested the presence of coherent infragravity wave energy alongshore.

Multivariate decomposition of the longshore runup signal extracted the important components of covariance among the transects. R-Mode analysis produced empirical factors with longshore amplitude patterns approximating the sinusoidal character of standing edge waves. Spectral analyses of factor scores revealed energy at different frequencies that could

satisfy the theoretical dispersion relation for several standing edge waves with longshore and cross shore modes (m,n). These spectral results agreed with spectra of a priori sinusoidal harmonics of the longshore runup that were extracted using spatial Fourier Filtering. Complex Empirical Orthogonal Functions were used to decompose the longshore signal while retaining frequency information in the factors. At least 9 low mode ($m=1,2$; $n=\leq 3$) infragravity standing edge waves from the 3 infragravitydominated days were revealed in the amplitude/phase signatures of the EOF factors. Individual edge waves contributed up to 4.6% of the total infragravity-band variance, and had shoreline amplitudes of 1.8-11.7 centimeters. In one instance, a mode $(m,n)=(1,1)$ accounted for 56% of the variance in the .002Hz wide band centered on .004Hz.

Calculation of the aspect ratio (longshore divided by offshore length scale) of each edge wave disclosed that in all cases modes extending well offshore beyond the surf zone dominated the edge wave field, substantiating the importance of turbulent surf zone damping of edge waves on dissipative profiles. Higher modes extending far beyond the headlands represented leaky mode energy partially standing in the cove with wavenumbers less than $m=1$. The diversity of observed modes (m,n) implies that an incident wave group forcing mechanism generates infragravity energy at a broad range of frequencies and length scales in the cove. However, broad peaks of energy in the Fourier and R-Mode spectra indicate the lack of a well-tuned resonanace at precise edge wave frequencies.

Standing Edge Waves On A Pocket Beach

by

Sara K. Culley

A THESIS

submitted to

Oregon State University

in partial fulfillment of
the requirements for the
degree of

Master of Science

Completed March 21, 1986

Commencement June 1986

APPROVAL:

Redacted for privacy

Associate Professor of Oceanography in charge of major

Redacted for privacy

Dean of College of Oceanography

Redacted for privacy

Dean of Graduate School

Date thesis is presented March 21, 1986

Typed by Sara Culley and Deb Jacobson for Sara K. Culley

ACKNOWLEDGMENTS

It was a tortuous path getting here from Virginia rivers to Swiss glaciers to the Pacific Ocean, but I always had the feeling I'd end up back at the beach where I always feel the best, watching and listening to the waves.

First, much gratitude is owed to the taxpayers of the United States for their generous support through a grant from the National Science Foundation. This research would not have been possible otherwise.

Thank you to everyone who has made me smile and been my friend over the last three years. Thanks to Karen Clemens for feeding me gummy bears and being a great office-mate, to Dave Murray for being one of the most cheerful people I know, to Pat Hays for keeping an even keel, and especially to Laurel for adding a great big spark to my day. I'll miss you all very much.

Deb put up with my thesis in good humor and talked about the outside with me. Steve kept the lab abuzz with epic tales about just about anything, and Tom was great to have around the lab listening to KFAT with me during the long days near the end.

The field work required a big effort from the whole gang. It couldn't have happened without Rob, Steve, Bob, Kevin, John, Peter, Holly, Paul K., and Paul O. You went all out for me, rain and shine, and we sure had fun doing it! Many thanks. I never did become an ace pool shark though.

Thank you to Dr. Robert Dolan for introducing me to Nearshore Processes at Virginia, and getting me fired up.

My deep appreciation to Dr. Vern Kulm for taking me to sea

and Peru. That was quite an adventure for me and I thank you for taking a chance on an untested polly-wog. I'll remember the roll of the waves and the flying fish a long time (not to mention the clams, of course).

The greatest thanks to my major professor and boss, Dr. Rob Holman, a very clever fellow who taught me not only the science, but the business of it all. I remember the first time I walked into his office for an impromptu interview and he simply said, "so what do you know, what can you do?". Of course, I figured I knew absolutely nothing, so I made something up about Bernoulli and wrote it on the board. It seemed to work, as I've been here ever since. I feel very fortunate to have enjoyed Rob's guidance and friendship. Have a good weekend Boss!

Special thanks to Bob for having so much fun tide pooling and beach combing with me in any weather, for training me to run compulsively for sanity, and for sharing the rough times too. Cheers to the future.

Thanks to my parents, Sara and Dave, for having undying faith in me whatever I do, for getting so excited about life, and for offering so many experiences to me. Thanks for the loose rein in the wild times even though it was tough; I wouldn't have made it through without you. Remember the Outback.

Finally, I dedicate this thesis to my sisters, Cindy, Mary Ellen, and Beth Ann because no one can take your place or make me laugh like a sister does.

TABLE OF CONTENTS

LIST OF FIGURES

LIST OF TABLES

LIST OF SYMBOLS

A	amplitude of Fourier harmonic of longshore runup signal
a	r-mode factor amplitude
a_l	r-mode factor score amplitude
a_n	amplitude of edge wave of mode n
a_e	measured shoreline edge wave amplitude
C	cospectrum
E	edge wave energy
e	constant
F	r-mode factor loading matrix
f	frequency in Hz
f	non-dimensional edge wave frequency
f	fundamental edge wave frequency on a bounded beach
G	discrete Fourier transform
g	gravitational acceleration
h	still water depth
HF	half-filter width
$H_{1/3}$	deep-water significant wave height
i	denotes complex term
k	refers to an r-mode factor
L_x	offshore edge wave length scale
L_n	Laguerre polynomial
L_y	edge wave wavelength
L	edge wave aspect ratio (L_y/L_x)
l	refers to an r-mode factor
lj	as subscript, pertaining to cross-spectral matrix elements and phase angle

m edge wave longshore modal number

N total number of transects alongshore

n edge wave mode

Q quadrature spectrum

R wave runup

$R_{1/3}$ significant runup height

S spectral estimate

T wave period

t time

t_j discrete time sample

T_R time series record length

$T_{1/3}$ deep-water significant wave period

U cross-spectral matrix

u cross shore edge wave velocity

v longshore edge wave velocity

X matrix of runup time samples from all transects

x cross shore coordinate

x_m eigenvector element

x_n eigenvector element

y longshore coordinate

y_i longshore position of transect i

α eigenvalue

Δ sample interval

β average linear beach slope

$\hat{\beta}$ best-fit linear beach slope

β_e effective beach slope

η sea surface displacement

Λ beach length

Θ phase angle

κ wavenumber

λ radial wavenumber

π constant

ρ density of water

σ radial frequency

σ_T^2 variance

Φ velocity potential

ϕ offshore edge wave behavior as a function of the Laguerre polynomial

ν degrees of freedom

L_n non-dimensional offshore distance of edge waves for Laguerre polynomial

STANDING EDGE WAVES ON A POCKET BEACH

CHAPTER I
INTRODUCTION

The importance of infragravity band (20-300 sec) wave energy in shaping the littoral environment has become apparent in recent years. Shoaling incident band (5-20 sec) waves are largely dissipated by breaking before reaching the shoreline, having reached a critical steepness as a function of wave height and period. Longer, less steep infragravity waves present in the nearshore do not oversteepen and break on typical nearshore profiles, so that a greater portion of the energy in this band is delivered to the shoreline as runup (the to and fro swash of the waves on the beachface). From wave runup studies under various deep water wave conditions, Guza and Thornton [1982] found that the portion of wave runup energy in the infragravity band varies linearly with incident wave height. In subsequent field studies during storms, infragravity energy dominated the nearshore wave field and the rearrangement of the littoral sediments [Holman and Sallenger, 1984].

During periods of high waves, when the infragravity band dominates the runup, large sedimentary features that repeat at regular intervals alongshore often develop in the nearshore with length scales from meters to kilometers [Aubrey, 1980]. On the Outer Banks of North Carolina, storms historically leave large

erosive embayments at regular longshore intervals [Dolan et al., 1979]. The fact that sand grains simply get pushed and deposited by the drift velocities of waves implies that longshore regularity is also present in the nearshore infragravity wave field when the rhythmic topography is formed [Bowen, 1972].

Infragravity-band edge waves are the most plausible explanation for the formation of rhythmic topography. Edge waves are surface modes trapped to the nearshore by refraction away from increasing water depth offshore, resulting in a net progression and periodicity alongshore. A maximum amplitude at the shoreline decays exponentially offshore after a number of zero crossings that define the mode, n, of the edge wave (Figure 1). The longshore-periodic drift velocities of edge waves would push sand into regularly repeating patterns alongshore. Recent models considering the origins of rhythmic topography focus on an edge wave mechanism [Bowen and Inman, 1971; Komar, 1973; Guza and Inman, 1975; Bowen, 1980; Holman and Bowen, 1982].

The first mathematical description of edge waves was formulated by Stokes [1846], who recognized only the lowest mode case where amplitude decays exponentially offshore. A century later, interest was revived when Eckart [1951] developed the shallow water solutions for a family of discrete modes on a plane beach defined by a dispersion relation between wave number and frequency, with Stoke's wave as the zero mode case. Ursell [1952] gave a full theoretical discussion of resonances for mixed spectra comprising forced and free modes under periodic forcing. Without recourse to the shallow water approximations, edge waves were

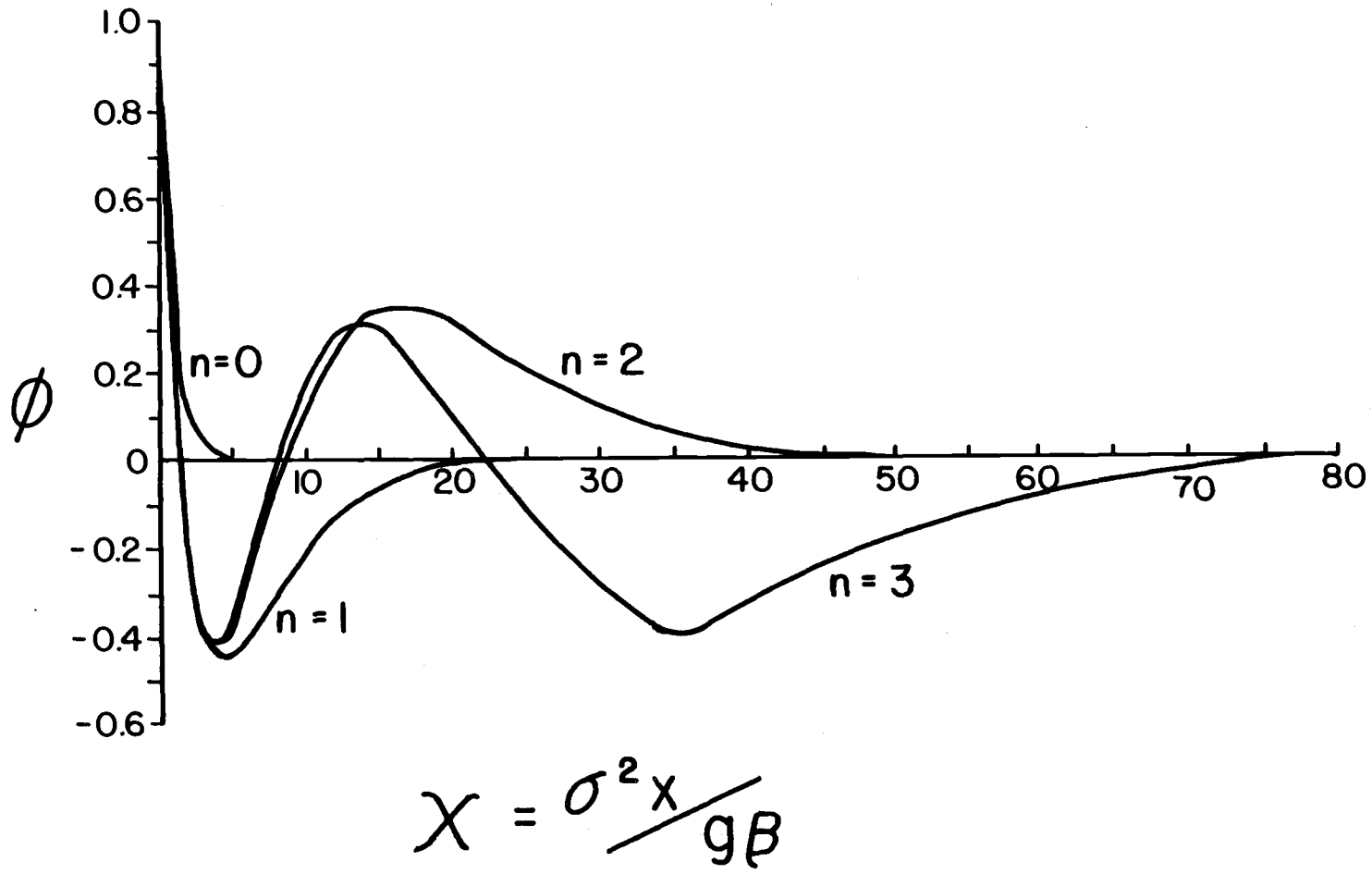

Figure 1. The offshore amplitude behavior for edge wave modes 0-3 as a function of non-dimensional offshore distance χ.

obtained as discrete free modes contained to the beach and extending furthest offshore at the cut-off frequency for each mode. Ursell's experiments in a laboratory canal measured resonant responses of edge waves by varying the forcing frequency to approach free modes predicted by the dispersion. He measured Stoke's edge wave for the first time. Ball [1966] generalized the solutions to an exponential profile. He found that the flattening profile offshore led to a low frequency cut-off for a given mode. He also confirmed that Eckart-Ursell waves make excellent approximations for low modes and low beach slopes when edge wave energy is contained very close to shore.

Higher frequency edge waves (on the order of incident waves) and the factors limiting their growth have been given much attention. On reflective laboratory beaches, Galvin [1965] and Guza and Inman [1975] reported resonant edge wave activity restricted to low turbulence conditions. In a wave basin, Bowen and Inman [1969] measured low mode synchronous standing edge waves arising from normally incident surging waves and noted that a single mode dominated the interaction. The relative importance of the modes was parameterized by a nondimensional ratio between the width of the surf zone and the offshore length scale of the edge waves. A correlation between the amplitudes of edge waves and the reflected standing incident wave suggested a resonant interaction.

Guza and Davis [1974] later explained that the standing incident wave is unstable with respect to two progressive edge wave perturbations, leading to resonant edge wave growth if the forcing function satisfies resonance conditions. The increased

turbulence of cleanly breaking waves was shown to suppress edge wave resonance, causing preferential excitation of modes with large offshore lengths, although the n=0 first subharmonic was the most easily excited mode for the laminar viscous dissipation of a very reflective system. Guza and Bowen [1976] later verified these arguments experimentally.

Shallow water, long period (1-5 minutes) waves, correlated with incident wave groups, were observed by Munk [1949] and Tucker [1950]. They each interpreted the waves as seaward-propagating free waves which they speculated were forced by variations of mass transport into the surf zone. Tucker recognized that the long wave trough accompanied the group crest. Longuet-Higgins and Stewart [1964] explained this 'surf beat' theoretically as a forced wave envelope travelling with the group, but 180^0 out of phase, balancing the excess mass transport of the modulating swell trains. They speculated that when incident breaking begins, the reflected forced wave could lead to second order free waves at the group frequency.

Gallagher [1971] developed a model for infragravity edge wave generation based on the surf beat concept. He derived a complicated function for nonlinear energy transfer from two modulating incident waves to a wave at the beat frequency. In this model the interaction mechanism is restricted to shallow water outside the surf zone. Resonant growth of free edge waves is predicted when the longshore components of group wavenumber and frequency combine to satisfy the theoretical dispersion.

Bowen and Guza [1978] simplified Gallaghers model and

considered free and forced modes in a realistic environment with breaking waves. Experimentally, modulating incident waves approaching the surf zone induced the greatest sea surface response under theoretical edge wave resonance conditions.

An alternate three-dimensional forcing model is [Holman, pers. comm.] based upon the radiation stress of breaking waves [Longuet-Higgins and Stewart, 1964]. In initial investigations of edge wave forcing dynamics, Gallagher's nonlinear forcing terms were found increasingly important toward the surf zone due to wave shoaling, making exclusion of the surf zone from the model unacceptable. In preliminary results, modulating wave trains in shallow water caused a periodic fluctuation in the breaker line position at any point alongshore and a periodic 'pulse' of excess momentum into the surf zone. From the spectrum of induced motions, progressive edge waves grew selectively as resonant free modes [Holman, pers. comm.].

There are few definite observations of edge waves in nature at surf beat frequencies. Huntley [1976] matched measured velocity decay and phase relations to a theoretical n=0 edge wave, and reported a series of discrete spectral peaks in reasonable agreement with predicted low mode progressive edge waves. However, his experimental design and others [Sasaki et al., 1976; Wright et al., 1979; Holman, 1981] lacked the longshore dimension necessary to delineate edge wave structure.

Katoh [1981] used aerial photography and Empirical Orthogonal Functions (EOF) to analyze wave runup adjacent to a breakwater. Longshore periodic motions were observed and

attributed to edge waves, but long and irregular frame intervals precluded definitive frequency analysis. From runup records at 14 transects over a 7 km distance alongshore on the Oregon coast, Holman and Bowen [1984] used complex EOF techniques to define a 5-10 km standing edge wave with a 140 second period. The wave accounted for about one-half the local significant runup height.

In the most conclusive demonstration of edge waves in nature, Huntley et al. [1981] used an extensive two-dimensional array of electro-magnetic current meters, extending offshore beyond the surf zone, to measure the nearshore velocity field. Two-dimensional power spectra in frequency-wavenumber space lined up on theoretical dispersion curves for progressive edge waves. Mode zero dominated at periods of 100-150 seconds, while large offshore length scales were evident for other energetic modes.

Most recently, Oltman-Shay and Guza [in press] extended upon the work of Huntley et al. [1981] with high resolution spectral estimators. On 15 days at two California beaches, frequency-wavenumber spectra were estimated for infragravity waves with longshore wavelengths on the scale of the array length. On all days progressive low mode edge waves ($n \leq 2$) accounted for 50%-90% of longshore current velocities, but corresponding modes in the cross shore currents were difficult to distinguish from leaky waves with the same wavenumber. The ratio of up to downcoast edge wave energy was within $1 \pm .2$ on 11 of 15 days and the energy contribution was correlated to the available amount of wind wave forcing of Gallagher's [1971] model.

The objectives of this study are to document edge wave

activity on a natural beach and to explore the edge wave climatology, including modal mix, strength of natural resonances, and relationships to the incident wave regime.

A field program was designed to gather this information. In four experiments under varying nearshore conditions, wave runup was measured along an entire beach using time lapse photography in conjunction with beach surveys. Time Series Analysis was used to examine the frequency and longshore wavenumber characteristics of the nearshore wave field, distinguishing low mode infragravity edge wave signals that satisfy the theoretical dispersion relation.

In Chapter 2 the edge wave kinematics are outlined with an emphasis on the application of standing edge wave resonances to this study. A description of the field site and procedure follows in Chapter 3. Chapter 4 presents the experimental results including offshore wave climatology, beach profiles, and wave runup spectra. In Chapter 5 three multivariate analysis techniques are explained and applied to the runup data. Fourier Filtering (5.1), R-Mode Factor Analysis (5.2), and complex Empirical Orthogonal Functions (5.3) address the nature of coherent longshore patterns in the runup signal. Chapter 6 is a discussion of the relationships between the edge wave modes and the nearshore environment. A concluding summary is given in Chapter 7.

CHAPTER II
EDGE WAVE KINEMATICS

From the linear, shallow water approximations to the equations of motion, Eckart [1951] derived the edge wave velocity potential to be

$$\Phi(x,y,t) = \frac{a_n g}{\sigma} \phi_n(x)\ f(y,t) \qquad (1)$$

Cross shore and longshore axes are represented by x and y, respectively, $\sigma=2\pi/T$ is the angular frequency of an edge wave of period T, and a_n is the amplitude of an edge wave of mode n. For the plane beach case with no longshore variations in slope (i.e. offshore water depth=f(x) only)

$$\phi_n(x) = e^{-\lambda x}\ Ln(2\lambda x) \qquad (2)$$

describes the offshore behavior as a function of the LaGuerre Polynomial, $Ln(2\lambda x)$, n=0,1,2...(Figure 1). $\lambda=2\pi/L_y$ denotes the edge wave radial wavenumber for an edge wave of length L_y.

The longshore sinusoidal periodicity is provided by

$$f(y,t) = \cos(\lambda y-\sigma t) \qquad (3a)$$

for a progressive edge wave, and by

$$f(y,t) = \cos \lambda y \cdot \cos \sigma t \qquad (3b)$$

for a standing edge wave alongshore. In a realistic environment, non-planar longshore profiles introduce changes in the behavior of λ and ϕ_n that in turn cause distortions in f(y,t) from the pure sinusoidal form.

The edge wave surface displacement at time t is

$$\eta(x,y,t) = -\frac{1}{g}\frac{\partial \Phi}{\partial t} = a_n \phi_n(x) f(y,t) \qquad (4a)$$

At the shoreline, edge wave displacement is reflected in the runup as

$$\eta(0,y,t) = a_n f(y,t) \qquad (4b)$$

with antinodes every y/L_y=0.0, 0.5, 1.0..., and nodes at y/L_y= 0.25, 0.75....

The corresponding cross shore edge wave current, u, and longshore current, v, are given by

$$u = \frac{\partial \Phi}{\partial x} = \frac{a_n g}{\sigma} \frac{\partial}{\partial x}\left[\phi_n(x)\right] f(y,t) \qquad (5a)$$

and

$$v = \frac{\partial \Phi}{\partial y} = \frac{a_n g}{\sigma} \phi_n(x) \frac{\partial}{\partial y}\left[f(y,t)\right] \qquad (5b)$$

Using (3b) for f(y,t),

$$v = \frac{a_n g\lambda}{\sigma} \phi_n(x) \sin\lambda y \cdot \sin\sigma t \sim \sin\lambda y \qquad (5c)$$

for the standing edge wave case.

The characteristic edge wave dispersion relation

$$\sigma^2 = g\lambda \sin[(2n+1)\beta]; \quad (2n+1)\beta<\pi/2 \qquad (6)$$

governs the modes, n, that are possible on a plane, low slope ($\tan\beta\sim\beta$) beach [Ursell, 1952], limited by the cut-off mode when $(2n+1)\beta=\pi/2$.

On real beaches the cross shore profile is generally not planar, but previous investigators [Oltman-Shay and Guza, in press] have demonstrated that a linear approximation of β is valid for low modes, n, on dissipative profiles of mild concavity. The appropriate range of slope may be determined using the "effective beach slope", β_e. Using a numerical model for edge waves on a typical, concave profile, Holman and Bowen [1979] found the best linear estimate of β to be

$$\beta_e = h(x')/x' \; ; \quad x' = 1/11(2n+1)L_y \qquad (7)$$

where h is the water depth at a distance x' from the shore. For low modes, n, β_e may be computed directly from profile data, but

for higher modes that extend offshore beyond the survey grid, β_e must be estimated from the flattening surf zone profile. It is important to bear in mind that β_e is an approximation of the actual complex profile that interacts with the edge wave modes.

From the dispersion relation, discrete, trapped modes arise whenever $\sigma^2 < g\lambda$. When $\sigma^2 > g\lambda$, so that (6) can not be satisfied, a continuous domain of untrapped, or "leaky" modes occur. An infinite number of possible σ,λ,n combinations exist to satisfy (6) for a particular beach. This makes it difficult to specify precise modes from spectral data.

Standing edge waves can be viewed as the sum of two progressive edge waves at the same frequency, 180^0 out of phase, travelling in opposite directions. This would occur, for example, on a beach bounded at both ends by reflective headlands with the boundary condition of no longshore current through the headlands ($v=0$ at $y=0$ and at $y=\Lambda$, where Λ is the beach length). From (5c), $v(x,0,t)=0$ and $v(x,\Lambda,t)=0 \rightarrow \sin\lambda\Lambda=0$, so that at the headlands standing wave displacement will always be at an antinode (i.e. a position of maximum runup excursion). This restricts λ in (6) to a discrete set of values given by $\lambda=2\pi\kappa=\pi m/\Lambda$. The dispersion relation changes to

$$f^2 = \frac{gm(2n+1)\beta}{4\Lambda\pi} \; ; \quad m=1,2,3... \qquad (8)$$

where $f = \sigma/2\pi$, $\kappa = \lambda/2\pi$, and m (the longshore modal number) is the number of half edge wave wavelengths that 'fit' into the beach

alongshore [Bowen & Inman, 1969]. For the standing edge wave case, β_e is easily determined from (7), using the modal number m to determine L_y. Figure 2 depicts the runup model for an m=2 standing edge wave.

Figure 3 is an f,κ-space presentation of (8), generalized to any beach. For $(2n+1)\beta << \pi/2$, (8) may be represented as

$$f^2 = g\beta/4\Lambda\pi * m(2n+1) = f_0^2 * m(2n+1) \qquad (9)$$

where f_0 is the fundamental edge wave frequency of any bounded beach. The nondimensional frequency $\hat{f}=f/f_0$ has been plotted in Figure 3 for different mode (m,n) combinations. Multiplication of $\hat{f}$ by a particular value of f_0 makes the illustration specific for a given beach.

Note that only particular (f,m) combinations are possible for a given standing edge wave mode, n; the number of possible (f,κ) combinations has been greatly reduced from the progressive wave case. This is especially so if we concentrate our analysis in the lower left corner (small m,n) of Figure 3 where very few standing edge wave possibilities exist.

The advantage of a sharper frequency response may also exist for the standing edge wave case. Assume that an edge wave of mode n is weakly forced across a broad band of frequencies and wavenumbers along a bounded stretch of shoreline. The topographic restrictions encourage resonance of the single frequency in the band that compliments n and the best fitting longshore mode, m, fixing m and f to satisfy (8) and "trap" the edge wave between the

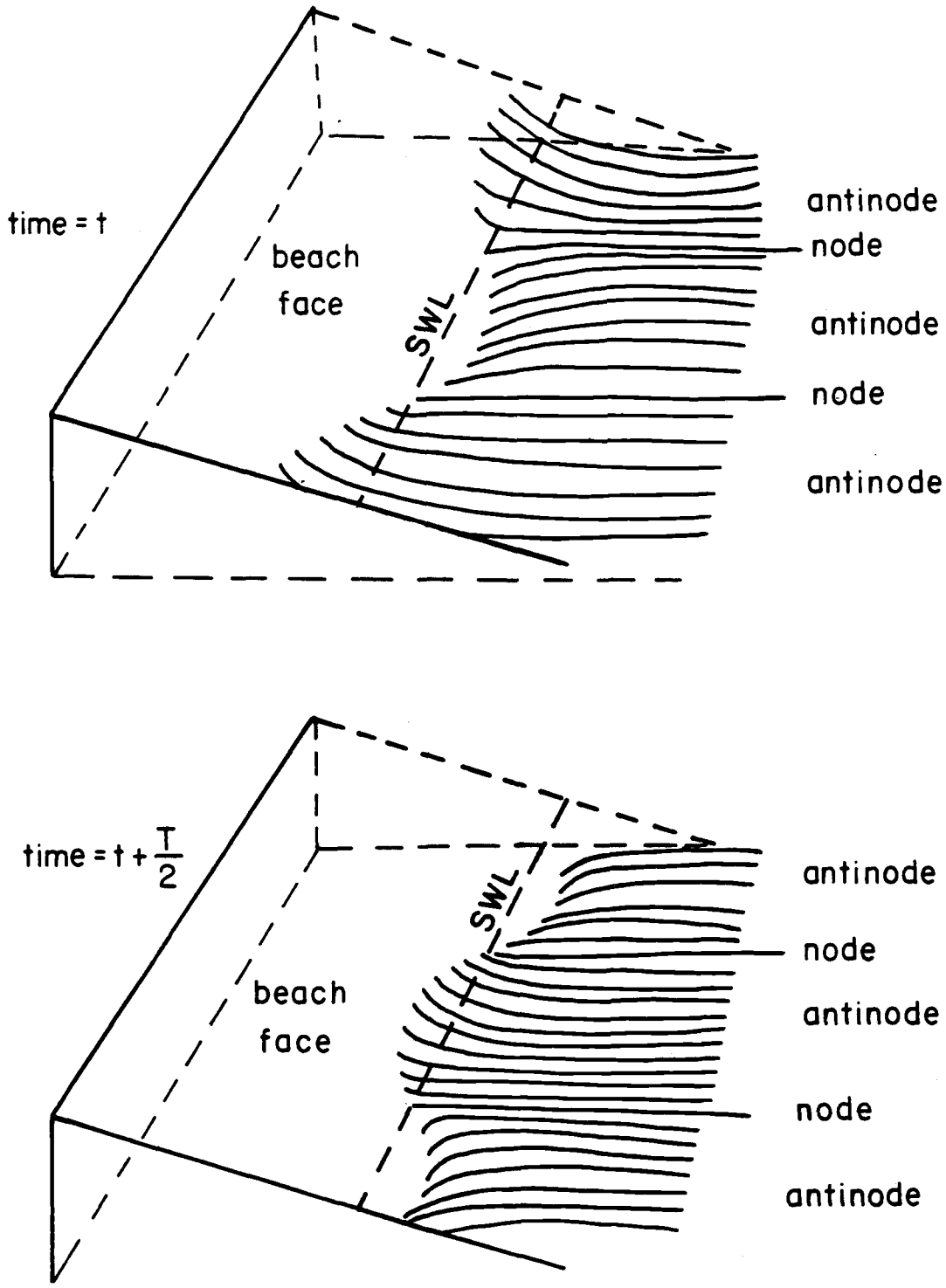

Figure 2. The runup pattern of a standing edge wave of longshore mode m=2 at time t, and one-half period later at t+T/2. The longshore boundaries may represent reflecting headlands.

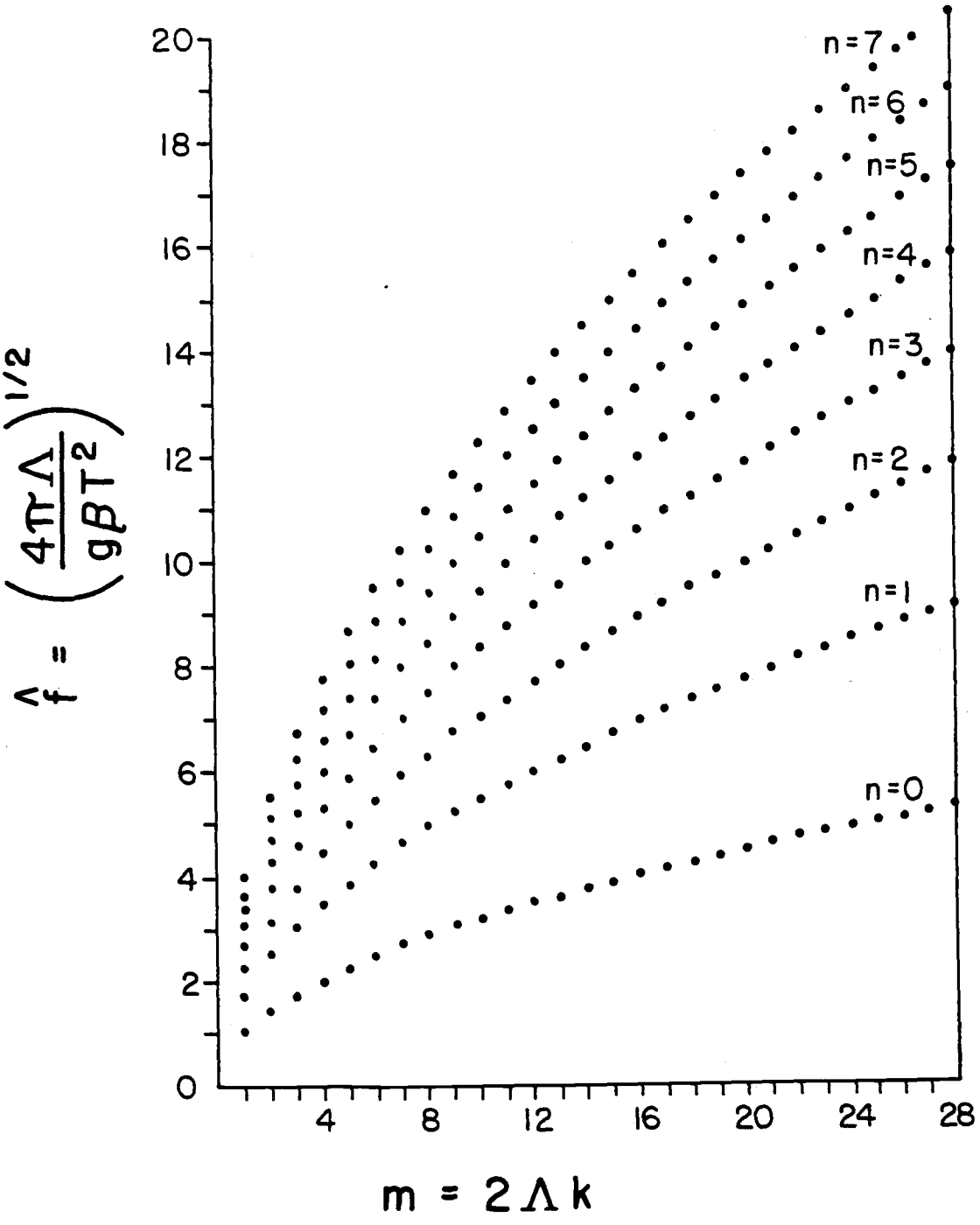

Figure 3. Non-dimensional frequency, wavenumber-space illustration of the standing edge wave dispersion relation.

barriers. For edge waves progressing along an open coastline, continuous possibilities of f,κ for any mode, n, provide no such tuning mechanism (6).

This investigation is designed to take advantage of the frequency selection provided by the topographically trapped standing edge wave model. An analogy can be drawn to the experiments of Ursell [1952] with controlled variation of a single forcing frequency until edge wave resonance was achieved. Spectral analysis of wave runup energy on a bounded beach may be expected to disclose well-tuned peaks of energy at predictable standing edge wave frequencies.

CHAPTER III
SITE AND EXPERIMENT

Field experiments were conducted on 02/26/84, 08/04/84, 10/26/84, and 02/02/85 (refered to as Days 1-4, respectively) at Short Sands Beach on the northern Oregon coast (Figure 4). The 800 meter long beach is bounded on the north and south by two large headlands that extend 800 meters and 500 meters offshore, respectively. The beach profile is strongly bimodal, divided into a steep, cobble back-beach, and a wider, dissipative beach and surf zone that has an average slope of about .02. The sharp break in slope between the two marked the landward limit of all wave runup considered in the experiments. The southwest orientation of the beach situates it well to receive large winter swells with typical incident wave heights of 1-3 meters, periods of 12-18 seconds, and mesotidal heights of 2-3 meters.

Time-lapse films of the swash zone recorded the runup signal along the entire beach length. Three Super-8 movie cameras were aimed alongshore from elevated positions behind the beach and on the headlands with each camera range covering a separate section of the swash zone alongshore. Three concurrent films were then shot bracketing the estimated high tide to minimize nonstationarity. Films with swash excursions entering the cobble back beach were rejected. A film length of 70 minutes and a frame interval of 2 seconds were designed to sufficiently resolve the runup frequencies of interest from .004Hz out to the Nyquist

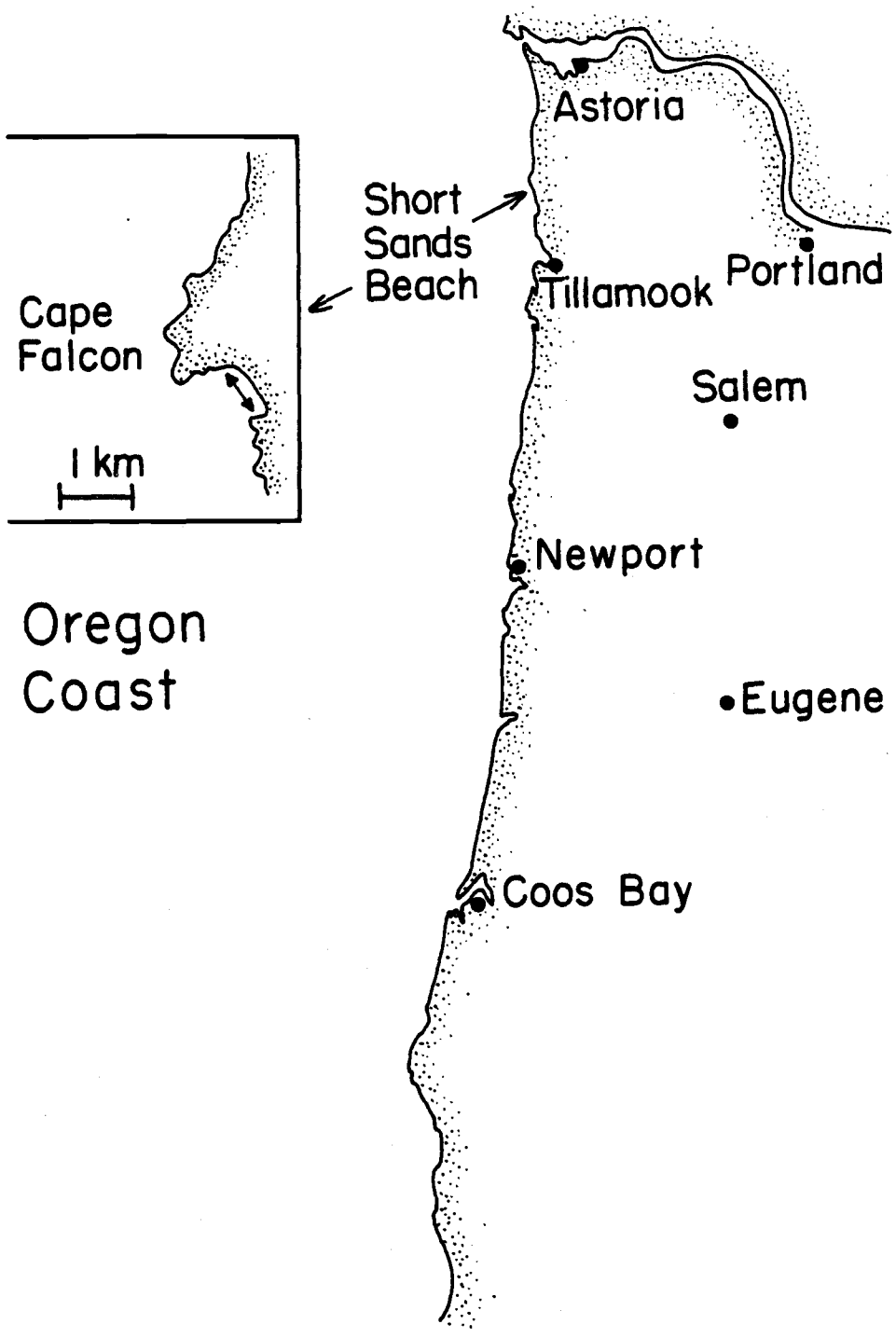

Figure 4. A map of the Oregon coast with a detailed view of the experimental site, Short Sands Beach.

frequency of .25Hz. Very small deviations in the frame intervals of each camera O(.0001 sec) were shown in laboratory tests not to drift over time.

In conjunction with the runup films, the low tide beach was surveyed with an OMNI Total Station using a laser beam reflected from a standard prism held at each grid point. The OMNI onboard computer mapped the point locations onto a standardized (x,y,z) coordinate grid for all four surveys. The large spring tidal ranges exposed much of the high tide surf zone to survey measurement.

The actual survey grids included 13-15 cross shore transects (beginning with A at the south headland) at 50-100 meter intervals alongshore, each extending seaward from the edge of the cobble beach. Exact transect positions were not reproduced for each survey. The transects and profile contours are shown in Figure 5, with the 0.0 meter contour corresponding to the mean runup elevation for each day. At each transect, a 10-meter long, bright orange flag was stretched across shore from the edge of the cobble while its landward and seaward ends were marked in the survey grid. Simultaneously, a camera, still in place from filming, recorded the flag position at the end of the swash film.

Using the developed films, the swash signal at each transect was digitized to generate concurrent time series of runup from along the entire beach. To digitize the runup, the film was projected up onto a ground glass table top and the transect positions were located from the orange flags that appear. The landward edge of the water was manually followed with a pointer

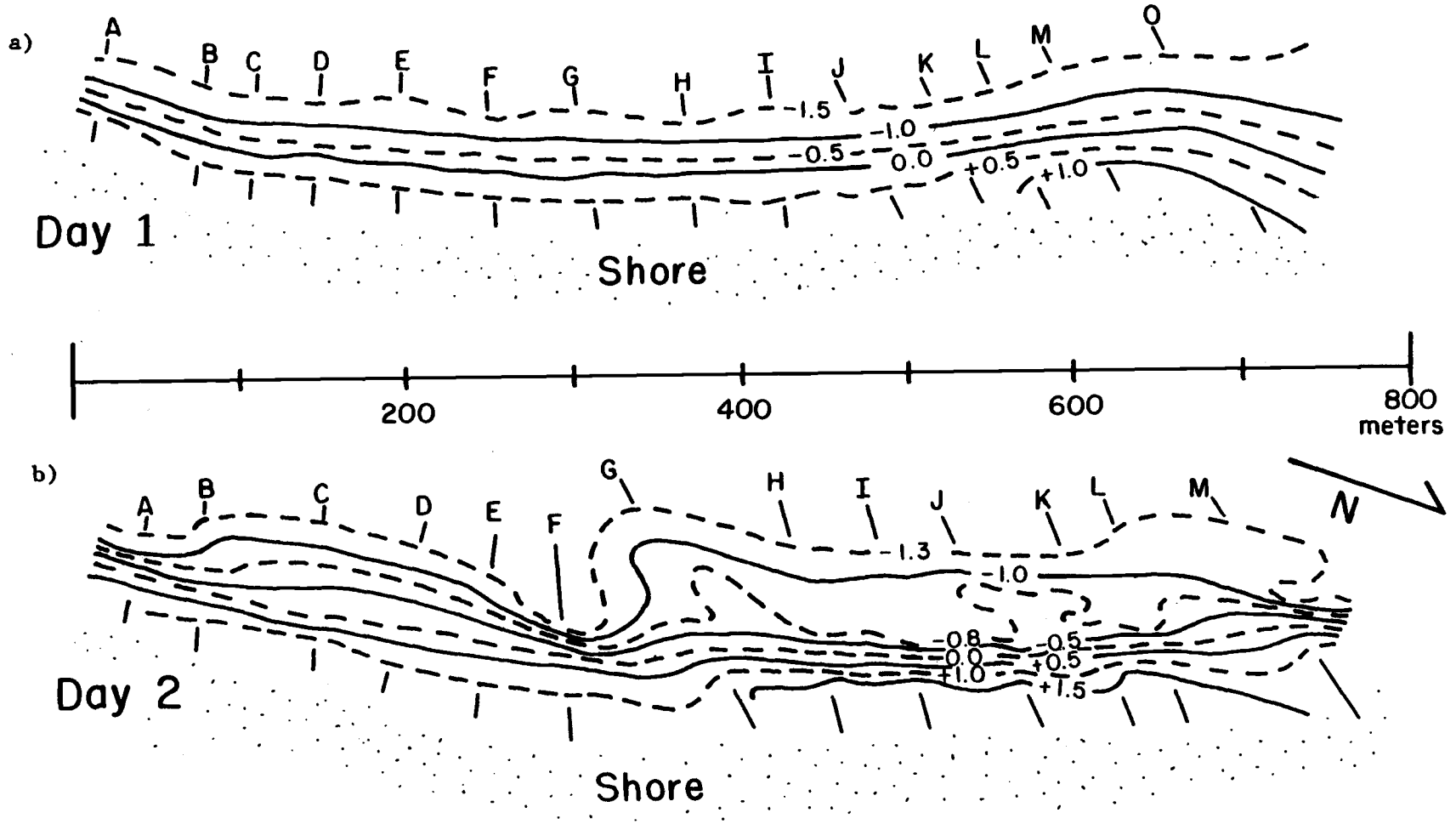

Figure 5. The beach profiles and runup transects for Days 1-4 (a-d). The 0.0 meter contour corresponds to the mean runup excursion on each day.

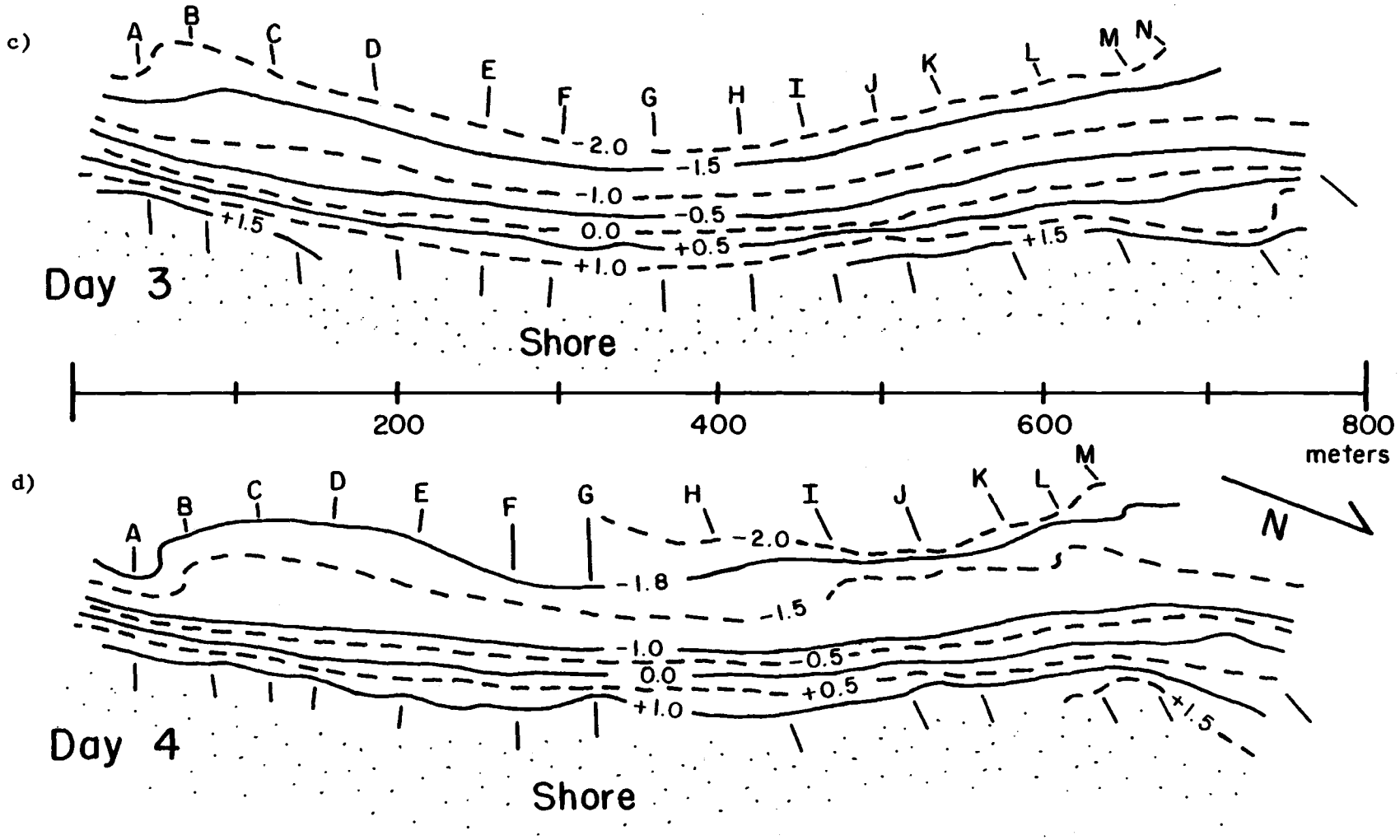

Figure 5 (continued).

that glided on a track lined up parallel to the transect orientation. As the film played, the pointer position was electronically digitized once during each frame. For each transect this scale was translated to meters by comparing the flag length in the digitized film to the actual surveyed length.

After digitization, the exact length of filming time and the known number of frames were used to interpolate the sample interval to precisely 2 seconds, allowing correct application of Time Series Analysis. Finally, the runup signal across the sloping beach was converted to vertical excursions using the transect profile information.

To evaluate operator error in interpreting the 'landward edge' of the swash, replicate digitizations of a runup time series at a single transect were analyzed. The average variance differed by at most 20%, with an average deviation of 8%. Spectra were essentially identical at frequencies below .04Hz [Holman and Guza, 1984].

The deep-water significant wave height ($H_{1/3}$) and period ($T_{1/3}$) were determined from an Oregon State University long-period vertical seismometer that rests on the floor at the Hatfield Marine Science Center in Newport, Oregon. The seismometer is calibrated to produce low-pass-filtered electrical signals proportional to the offshore (about 2 km) wave height. The pen arm of a chart recorder connected to the seismometer responds to the signals and draws a time series of the fluctuating water level [Creech, 1981]. $H_{1/3}$ and $T_{1/3}$ were computed directly from the strip charts. A summary of conditions is listed in Table I.

CHAPTER IV
OBSERVATIONS

4.1 Nearshore Environment

A typical transect profile from each of the four beach surveys is plotted in Figure 6 along with the average beach slope (β) of each, computed as the average slope of the entire surveyed profile. On all days, the beach steepens slightly to the south and has a flatter embayment centered at 300 meters (Figure 5).

The profiles for Days 1, 3, and 4 are mildly concave and dissipative with β varying between .013 and .025, steepening landward. On these days the surf zone bar systems were not well developed and the topography was fairly uniform alongshore. Incident breaking waves were longcrested and plunging-spilling except where breaking was inhibited by a moderate, 0.5 m/s (visual estimate) rip current at 250 meters.

The August profile of Day 2 has a dissipative surf zone and a reflective (β=.05-.06) high tide swash zone that intersect at a sharp break in slope along most of the beach. A longshore trend in the profile on Day 2 reflects the emergence of a bar that extended from the base of the swash zone at 319 meters to the north headland about 150 meters from the shoreline. This 'half-crescentic bar' was visible with waves spilling onto the seaward side. Not noticeable from the contours (Figure 5b) are the beach cusps of approximately 20-meter wavelength that formed the reflective swash berm on Day 2. Very low amplitude surging

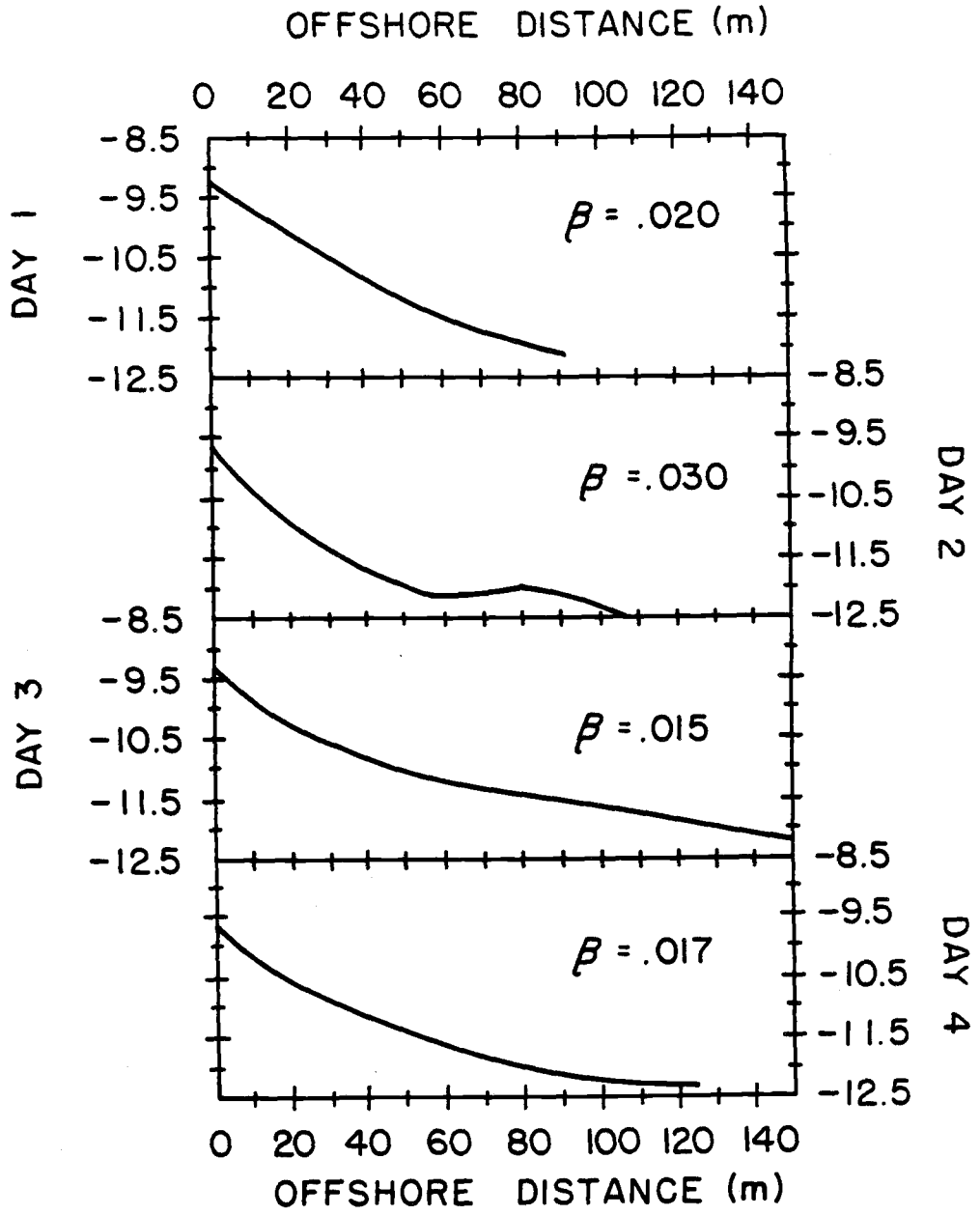

Figure 6. A typical transect profile from each day including the average linear slope, β.

waves were present in the inner surf zone, longshore currents were not noticeable, and the rip current was not active on this day.

4.2 Runup Spectra

The distribution of variance with frequency in each runup time series of length $T_R\Delta$ (where T_R is the total number of samples) is expressed with the Discrete Fourier Transform (G) by

$$G(f) = \frac{1}{T_R} \sum_{j=1}^{T_R} R(t) * e^{-i\left(\frac{2\pi n t_j}{T_R}\right)} \qquad (10)$$

where R(t) is the runup at time t_j, and f is the Fourier frequency, $n/T_R\Delta$, for integer n and sample interval Δ. The one-sided spectral estimate

$$S(f) = 2T_R\Delta\ G(f)G(f)^* \ ;\ (n=0,\ldots,T_R/2) \qquad (11)$$

measures the portion of runup variance in the time series that oscillates with frequency f. $G(f)^*$ denotes the complex conjugate of G(f). The raw spectral estimates were smoothed with a Tukey Filter which computes a running average of S(f) over a desired number of estimates. The number of degrees of freedom in the smoothed spectrum are $\nu=8/3(HF-1)$ where HF is the half-filter width. The bandwidth for this filter is $\Delta f=4/3(Hf-1)*1/T_R$ [Jenkins and Watts, 1968].

In Appendix 1 (Figure A1.1) the spectra are shown with ν=77 out to the Nyquist frequency of .25Hz. Notice the logarithmic decay of variance to insignificant values at frequencies greater than .10Hz on all days. In Figure 7 the spectra are computed out to 0.1Hz (ν=24), covering the incident-infragravity range where virtually all of the runup variance occurs. The spectra for each digitized runup film are stacked from south (bottom) to north (top), with labels corresponding to the transect labels in Figure 5. The vertical offset, dy, appears on each Figure 7(a-d), and the total variance (σ_T^2) and significant runup height ($R_{1/3}$= $4(\sigma_T^2)^{1/2}$) appear on the right of each spectrum. A bar at the top of the figures marks the general range of frequencies that are relevant to the standing edge wave model (8) for low modes (m,n) on dissipative profiles. Table I summarizes the spectral statistics and the offshore wave data.

There are systematic differences between the wave energy of Days 1, 3, and 4, and that of Day 2. Infragravity (.003Hz-.05Hz) energy dominates the runup for Days 1, 3, and 4, where an average of 97%, 95%, and 98%, respectively, of the variance is below .05Hz. In contrast, an energetic band from .05Hz-.07Hz dominates Day 2 leaving on average 52% of the variance below .05Hz. In the frequency range .005Hz-.02Hz, the variance on Day 2 is 5-100 times less than that of the other days. Also, Days 1, 3, and 4 have larger overall runup variances and deep-water incident wave heights than Day 2. The focus of consideration in the next chapters will be on the infragravity-dominated Days 1, 3, and 4.

On these days spectral peaks consistently reappear near

TABLE I

Summary of offshore wave conditions and wave runup spectra for Days 1-4. Included are deep water wave height ($H_{1/3}$), incident wave period ($T_{1/3}$), mean total runup variance of all transects alongshore ($\overline{\sigma_T^2}$), mean significant runup height of all transects alongshore ($\overline{(R_{1/3})}$), and the mean percent of σ_T^2 at frequencies below .05Hz ($\%\sigma_T^2$<.05Hz).

	Date	$H_{1/3}$(m)	$T_{1/3}$(s)	$\overline{\sigma_T^2}$(m^2)	$\overline{R_{1/3}}$(m)	$\overline{\%\sigma_T^2}\leq$.05Hz
Day 1	02/26/84	2.5	15	.025	0.63	97
Day 2	08/04/84	0.5	12	.017	0.51	52
Day 3	10/26/84	1.0	14	.083	1.15	95
Day 4	02/02/85	3.0	13	.109	1.32	98

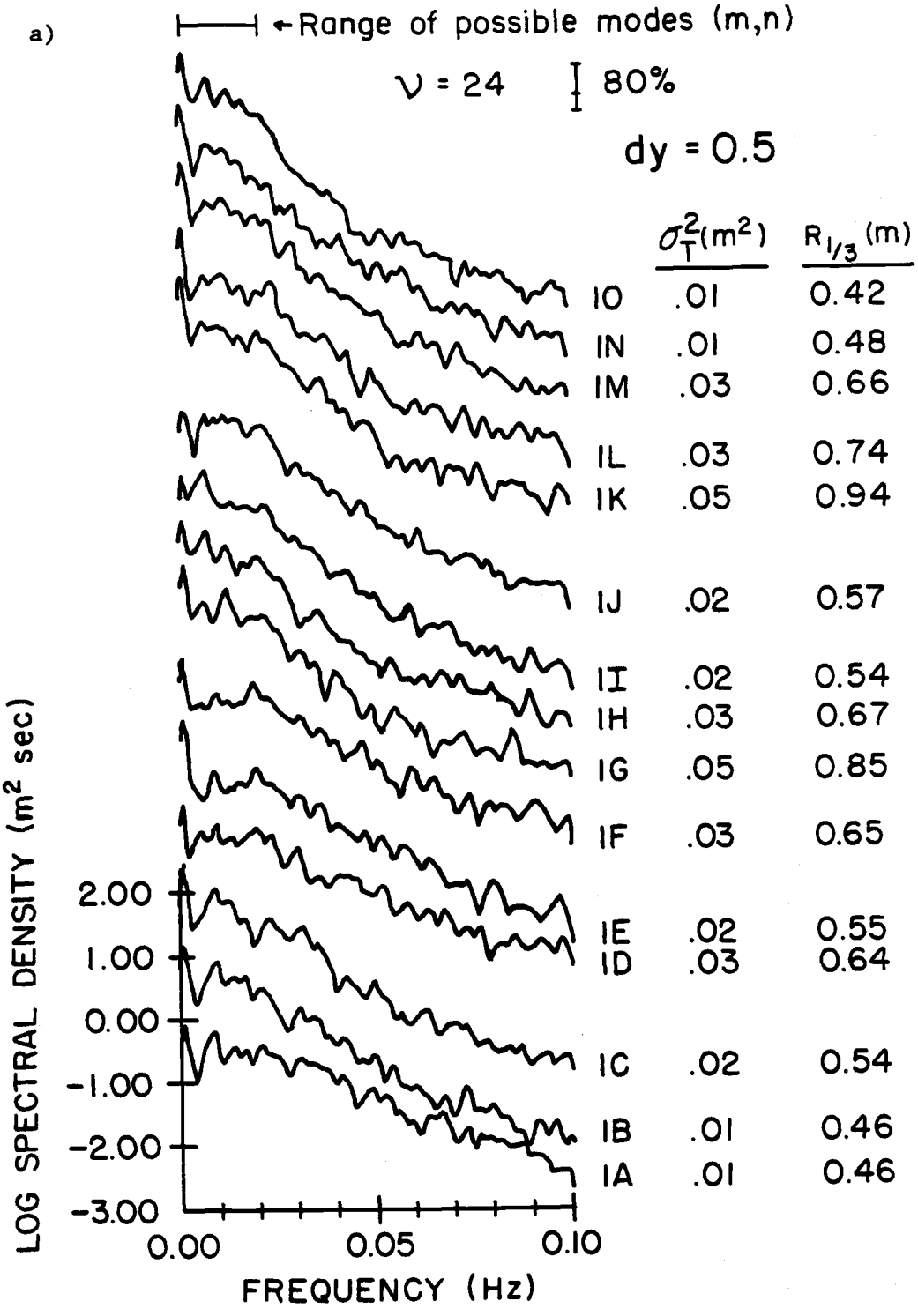

Figure 7. Spectra of runup for Days 1-4 (a-d), stacked from south (bottom) to north (top) with labels corresponding to the transects in Figure 5. The vertical offset is given by dy.

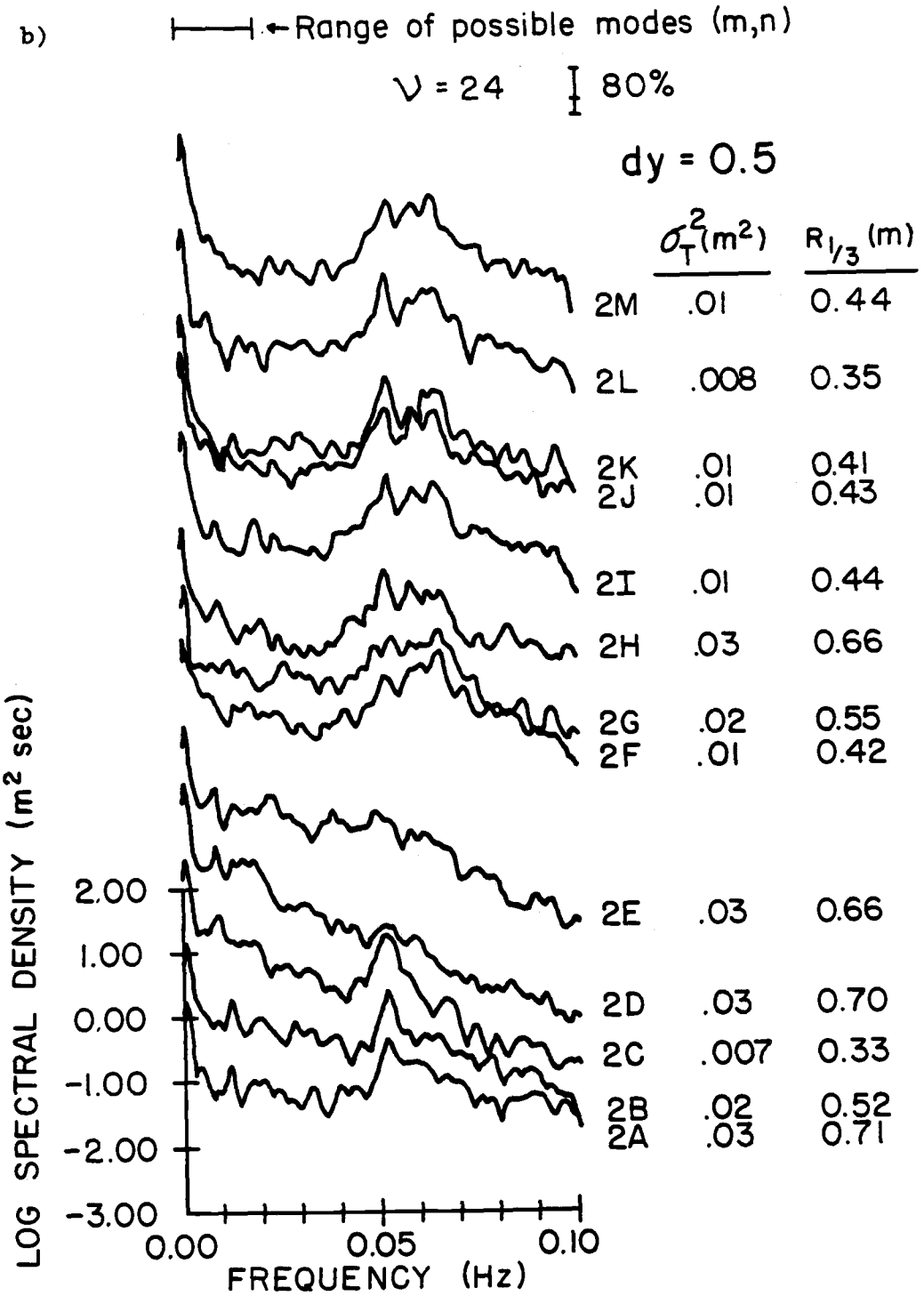

Figure 7 (continued).

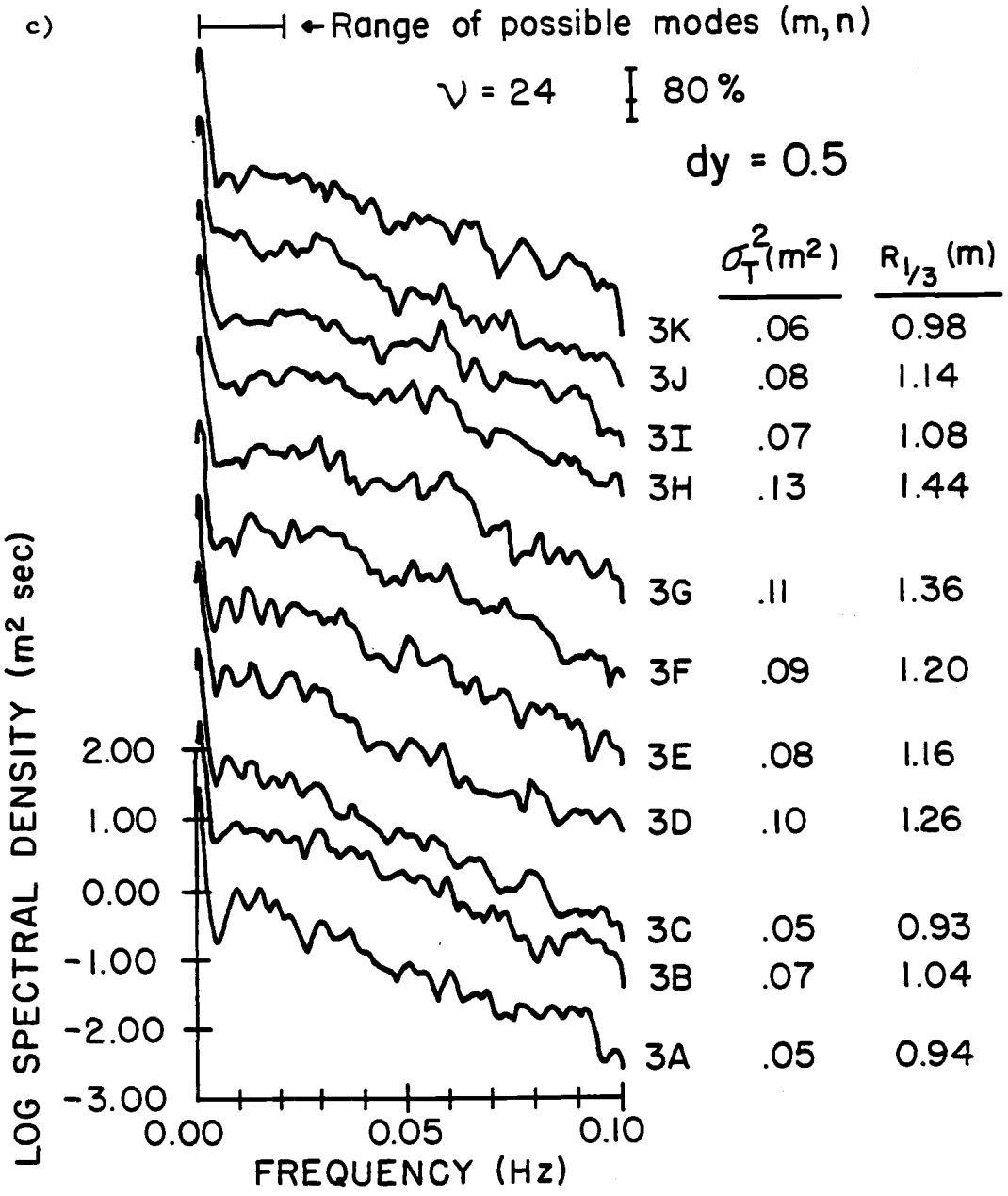

Figure 7 (continued).

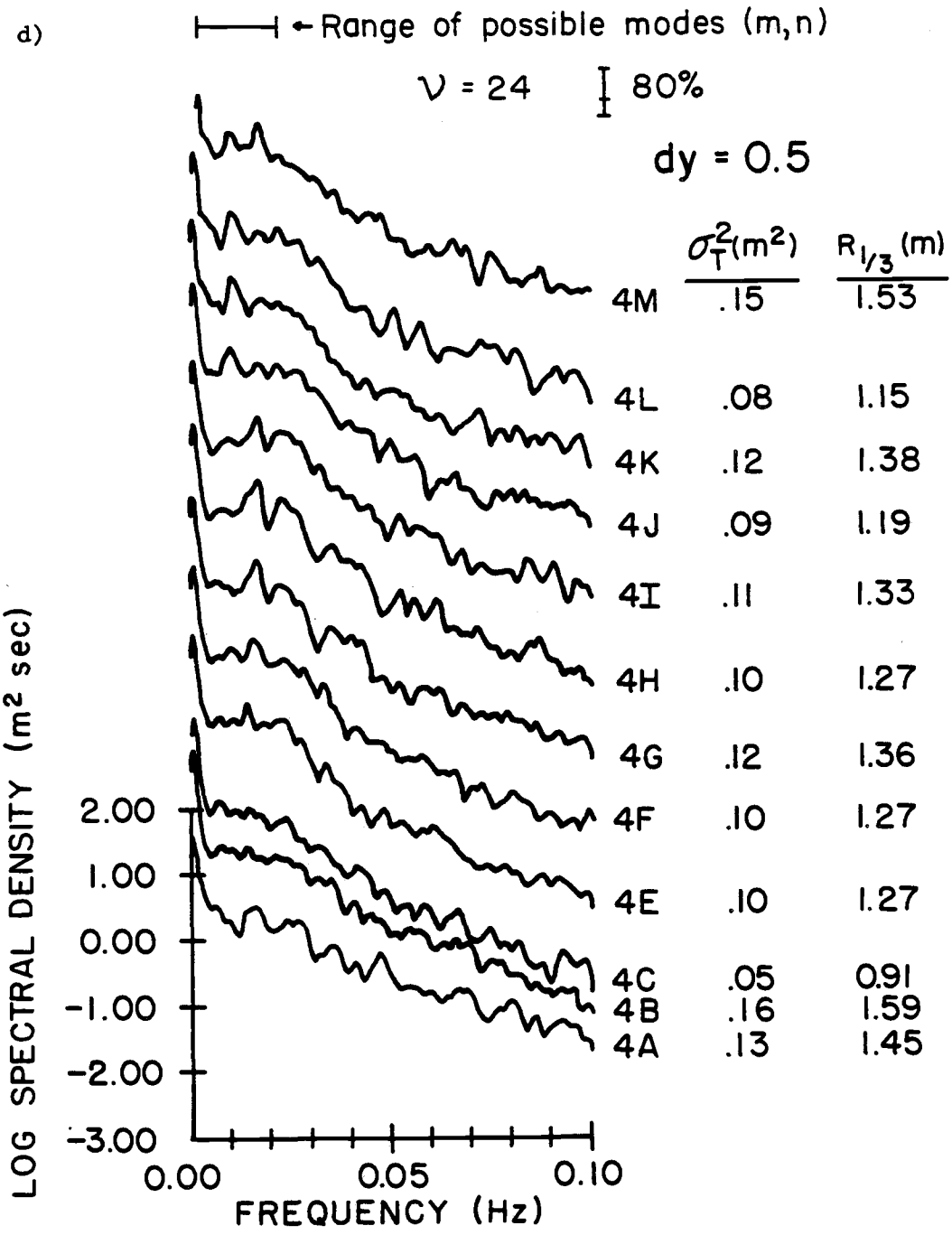

Figure 7 (continued).

.01Hz (Figure 7). Interesting patterns are evident with energy varying between peaks and valleys alongshore. For example, on Day 1 (Figure 7a) a peak at .007Hz-.01Hz at the south end of the beach (Transect A) declines steadily toward the north, falling to a valley at mid-beach (Transect G), and then rising again to a peak at the north headland (Transect O). An intriguing comparison can be made to the antinode-node character of runup of a standing edge wave with longshore mode m=1.

Conclusions about edge waves in the nearshore wave field drawn from these spectra alone would not be very informative. The spectral peaks are broad and it is not terribly obvious whether a true correspondence to different edge wave modes (m,n) exists at particular frequencies. Also, the overlap in frequency of many modes (m,n) leaves the choice of edge wave modes non-unique. In the next chapter, with attention centered on the topographically-trapped standing edge wave model, m modes will be extracted from the spectra with multivariate methods that can illucidate coherent relationships alongshore in the runup.

CHAPTER V
MULTIVARIATE ANALYSES

5.1 Fourier Filtering

Filtering of the longshore runup signal by Fourier Analysis was used to investigate possible long waves standing in the cove. The technique decomposes the longshore wavenumber spectrum of runup variance into a set of sinusoidal harmonics. The Fourier series approximation of the runup signal, R, at time t_j and transect position y_i, is given by

$$R(y_i,t_j) = 2 \sum_{m=0}^{\infty} A(m,t_j) * \cos\left[\frac{m\pi y_i}{\Lambda}\right] \qquad (12)$$

where m is a harmonic of the fundamental longshore wavenumber, A is the amplitude of each harmonic, and Λ is the beach length (equal in all cases to 800 meters) [Kaplan, 1981]. This infinite sum over m reproduces the total original variance, and a model of a single longshore harmonic, m, of the runup signal is obtained as

$$A(m,t_j) = \frac{2}{N} \sum_{i=1}^{N} R(y_i,t_j) * \cos\left[\frac{m\pi y_i}{\Lambda}\right] \qquad (13)$$

where $A(m,t_j)$ is a new time series that retains the portion of total runup variance that oscillates with longshore wavenumber m, and N is the total number of transects.

The full Fourier expansion was reduced to a cosine series for this application, simplifying the logistics so that cosine maximums occur at $n\pi$ (n=0,1,2...) phase alongshore (i.e. model antinodes occur at the headlands).

Figure 8 depicts the runup model for the first two harmonics (m=1 and m=2). Each harmonic approximates the pattern of a standing edge wave of longshore mode m, and may contain energy from several free edge wave modes, n, at different frequencies. To gain independent evidence for the possible standing edge wave modes (m,n), spectral analysis was carried out on model time series A(m,t) for harmonics m=1,2 for the infragravity-dominated Days 1, 3, and 4.

Results for models $A(1,t_j)$ and $A(2,t_j)$ are shown in Figure 9. The spectra (to .02Hz) are overlain by bands marking the frequencies that could satisfy (8) for different modes (m,n) for the values of effective beach slope (βe) listed in Table II. By separating the modes, m, with this model, overlap of possible combinations (m,n) was eliminated at a given frequency, simplifying the discrimination of edge wave modes to a tractable problem.

In both Figures 9(a,b) many spectral peaks occur at frequencies that correspond to different standing edge wave modes (m,n). For example, on Days 3 and 4, (m,n)=(1,0) (Figure 9a) is centered on the peak at .004Hz. Also, there is a recurrance of some spectral peaks on all three days, such as (m,n)=(1,1) in Figure 9a. In Figure 9b, (m,n)=(2,1) matches a peak that shifts from .011Hz on Day 1 to .010Hz on Days 3 and 4, very possibly due

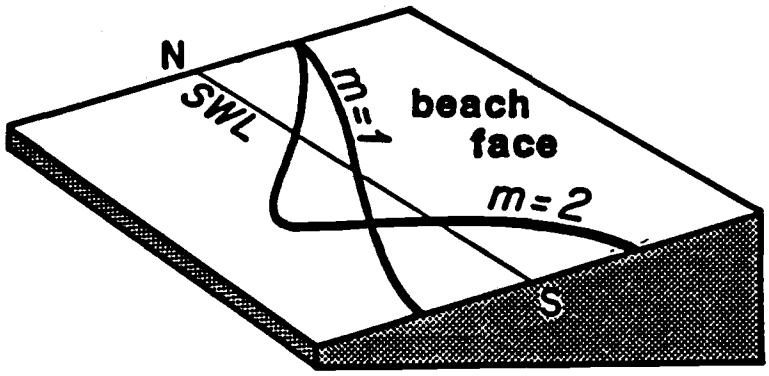

Figure 8. A model of the longshore runup pattern of the Fourier harmonics m=1,2, obtained by Fourier Filtering of the longshore runup signal. These modes approximate the runup pattern expected for standing edge wave modes m=1,2.

TABLE II

Effective beach slope (β_e) for each mode (m,n) on Days 1-4, as computed from (7). For n>3 β_e was estimated to be constant from the flattening profile offshore.

n	β_e							
	Day 1		Day 2		Day 3		Day 4	
	m=1	m=2	m=1	m=2	m=1	m=2	m=1	m=2
0	.025	.035	.050	.055	.018	.023	.018	.021
1	.017	.020	.040	.045	.015	.015	.015	.015
2	.017	.017	.035	.040	.015	.015	.015	.015
3	.	.	.	.	.	.	.	.
	.	.	.	.	.	.	.	.
	.	.	.	.	.	.	.	.

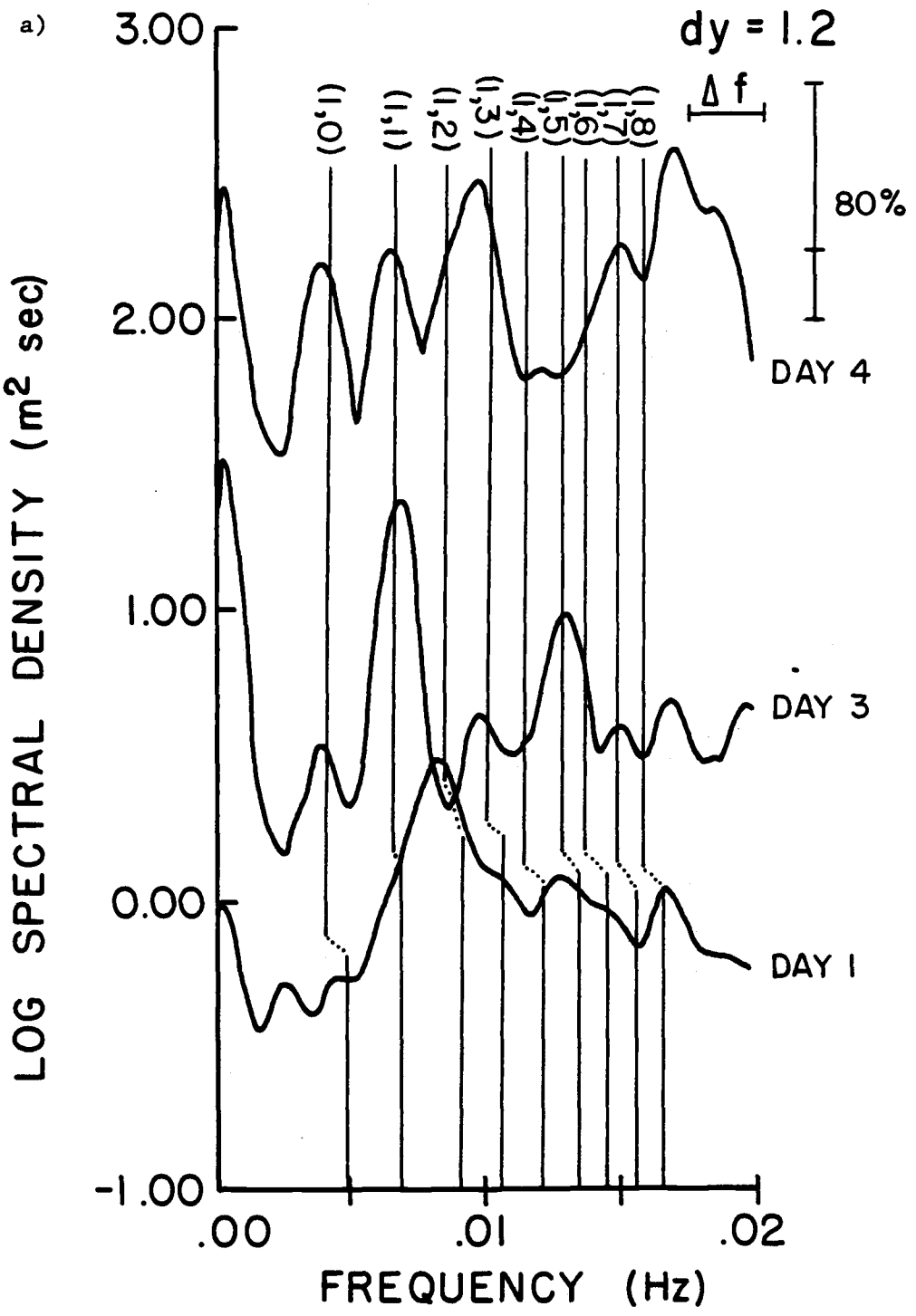

Figure 9. Spectra of runup for Fourier harmonics a) m=1 and b) m=2. Bands mark frequencies satisfying the edge wave dispersion relation for a) modes (m,n)=(1,n) and b) (m,n)=(2,n).

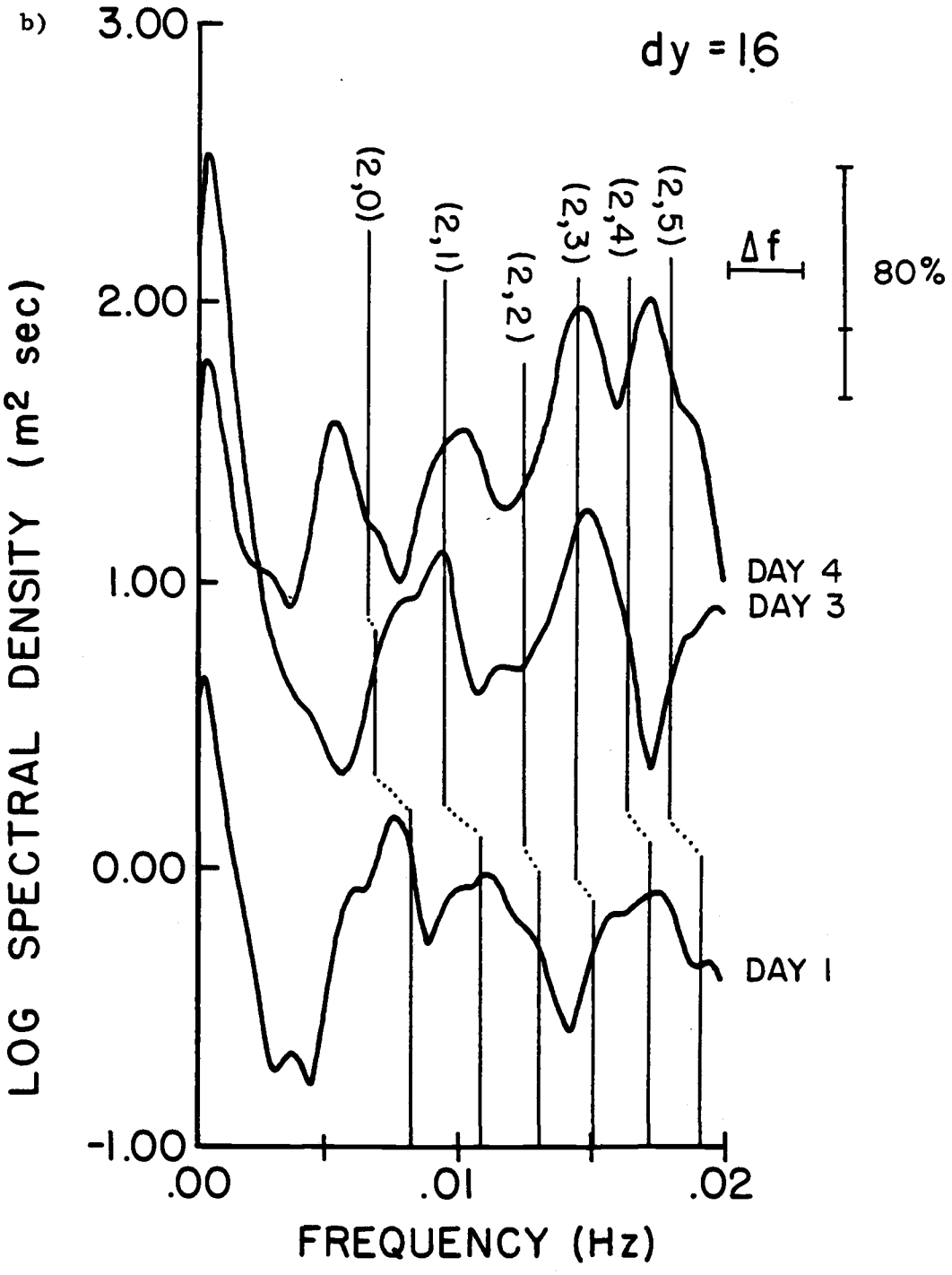

Figure 9 (continued).

to the different beach profiles (Table II). This could suggest the common reappearance of similiar infragravity wave motions at Short Sands Beach. However, the spectra are not conclusive; in all cases variance is broadly distributed without very sharp peaks.

A limitation of this sinusoidal model could provide an explanation for the weak peaks. From (3b), the longshore behavior of an edge wave is exactly sinusoidal only when the nearshore profile has no y-dependence (i.e. $\beta e=f(x)$ only). This is rarely true on a real beach, so that f(y,t) generally approximates a sinusoid, with distortions that reflect the irregular topography. For a standing edge wave on this irregular beach, only the portion of its variance that fits a sinusoid will be extracted by the model (using (13)), along with a certain amount of other variance (probably incoherent alongshore) at time t_j. The spectrum of $A(m,t_j)$ will provide a minimum estimate of the edge wave variance, and for a distorted f(y,t) random energy at other frequencies could dominate the spectrum and obscure the edge wave signal. For example, broad "zones" of high energy on Day 1 (Figure 9b) cloud possible edge wave peaks for low modes (m,n).

In the next section, R-Mode Factor Analysis will be used to decompose the actual edge wave modes, m, without the problematic sinusoidal simplification.

5.2 R-Mode Factor Analysis

The goal of R-Mode Factor Analysis is to simplify the

information in a multivariate data set. The technique is widely applied in geology to the understanding of such diverse topics as marine fossil assemblages [Pisias, 1978] and igneous petrology [Pearce, 1976]. The components of covariance among the variables are represented by more elementary, linear combinations of the original variables. The samples at time t, of N transect variables, $X_n(t)$, can be decomposed into N orthogonal factors, $F_k(n)$, by

$$X_n(t) = \sum_{k=1}^{N} a_k(t) * F_k(n) \qquad (14)$$

where a is the amplitude of factor k at time t [Davis, 1976]. The R-Mode orthogonal expansion (like the Fourier modes) has the property that the factor amplitudes are uncorrelated over time. However, unlike a priori Fourier modes, R-Mode factors are derived empirically.

This transformation is the most efficient way to view the total variance, as it minimizes the sum of squared errors and retains the variance-covariance structure of the data, assuming a multivariate normal distribution of variance. The new factors may be thought of as N orthogonal axes (new variables), each representing an independent end-member of covariance, whereas the original N axes (original variables) are interrelated, obscuring the essential nature of covariance. To maintain orthogonality each factor has a different number of zero crossings than the preceeding (greater percent variance explained) factor, and

variance is distributed equally about the zero crossings.

The canonical expression for the problem is

$$\sum_{n=1}^{N} \{x_m, x_n\} F_q(n) = \alpha_q F_q(m) \qquad (15)$$

where $F_q(n)$ are the eigenvectors of the symmetric correlation matrix with elements $\{x_m, x_n\}$, and α_q are the corresponding eigenvalues [Davis, 1976]. The normalized elements of each eigenvector, $\alpha_q F_q(n)$, make up the Factor Loading Matrix which reflects the portion of variance from each transect, n, that is accounted for by Factor 1_q. The total variance explained by each factor is obtained as the ratio between its eigenvalue, α_q, and the trace of the correlation matrix. The original time samples of runup at all transects $X_n(t)$ are mapped onto the new orthogonal factors at each time t as

$$a_q(t) = \sum_{n=1}^{N} X_n(t) F_q(n) \qquad (16)$$

Factor Scores are generated as transformed time series, $a_q(t)$, of the runup amplitude that fits the longshore signature of each independent factor F_q.

To provide a control for R-Mode decomposition of the wave runup on Short Sands Beach, R-Mode Analysis was performed on synthetic white noise time series at 15 hypothetical transects alongshore. Results for the first 3 factors are shown in Figure 10 along with the percent of total variance explained by each.

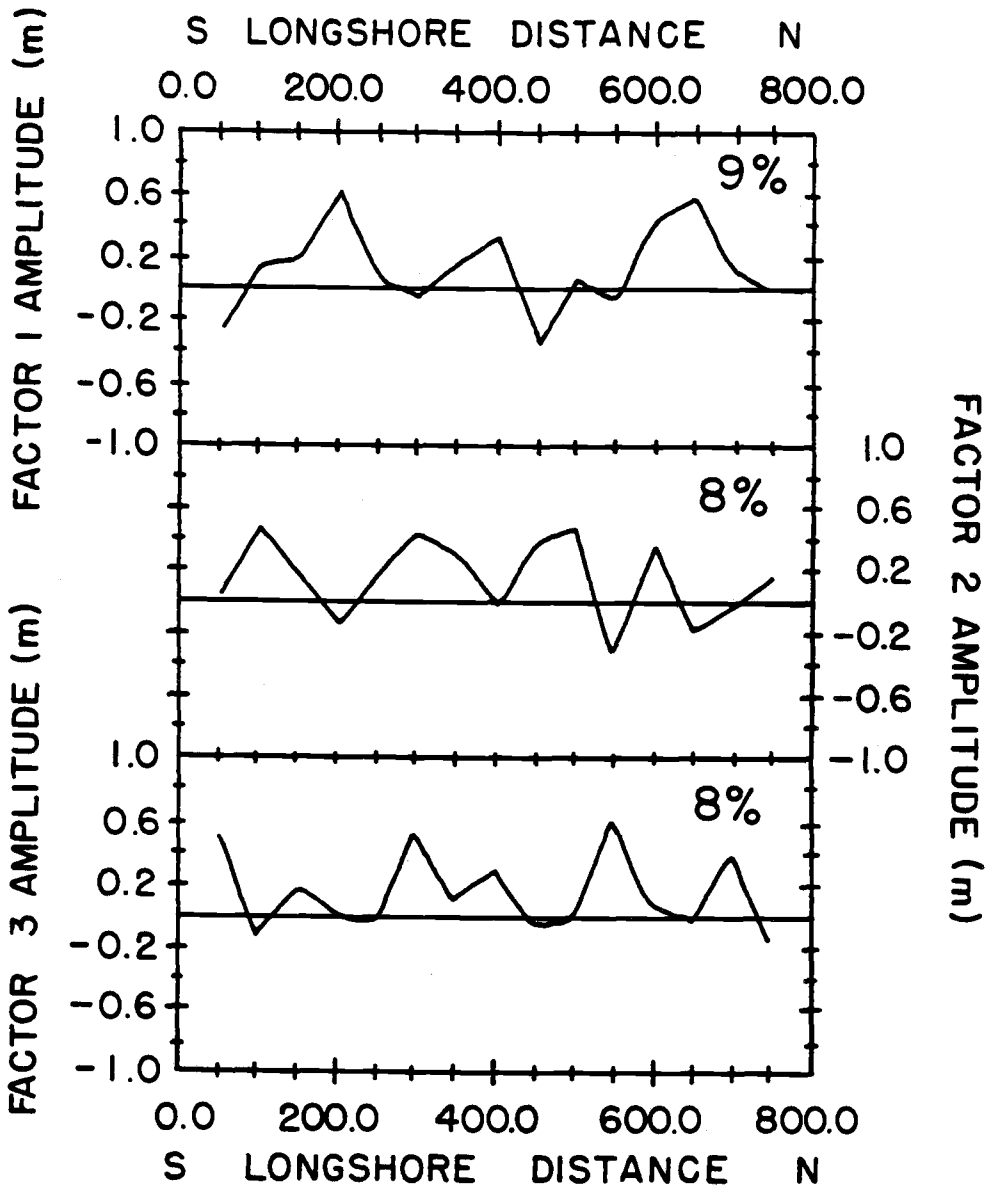

Figure 10. R-Mode Factors 1-3 of the runup pattern of 15 synthetic white noise time series at 15 hypothetical transects alongshore. The percent of total variance contributed by each factor is included.

The Factor Loadings appear random, and none of the three resemble the roughly sinusoidal pattern expected for a standing edge wave present in the longshore runup signal. A total of 15 factors (each contributing 8-6% of the total variance) were required to explain essentially 100% of the runup variance. This indicates that a more efficient representation of the 15 original variables was not gained via the R-Mode decomposition. Physically, these results demonstrate the lack of important sources of covariance between the variables (i.e. there are no important coherent patterns in the longshore runup signal). This is consistent with the random nature of the input time series.

In another test the real runup time series from Short Sands Beach (Day 3) were decomposed into factors after being scrambled among their actual transect positions (Figure 11). For most applications the ordering of the variables is irrelevant to the interpretation of the factors, whereas in this study the proper transect (variable) order is essential to the definition of a wave pattern alongshore. Therefore, no physical reason exists for the erratic Factors 2 and 3 in Figure 11 to resemble a standing wave pattern. Instead, they may serve as a control for the actual R-Mode results, giving validity to correctly ordered factor patterns that do suggest standing edge wave motions.

The Factor Loadings at each transect position alongshore for the first three R-Mode factors on all days are plotted in Figures 12-15, along with the percent of total runup variance contributed by each factor. Only the three dominant components were retained in order to avoid nonphysical reconstructions that commonly occur

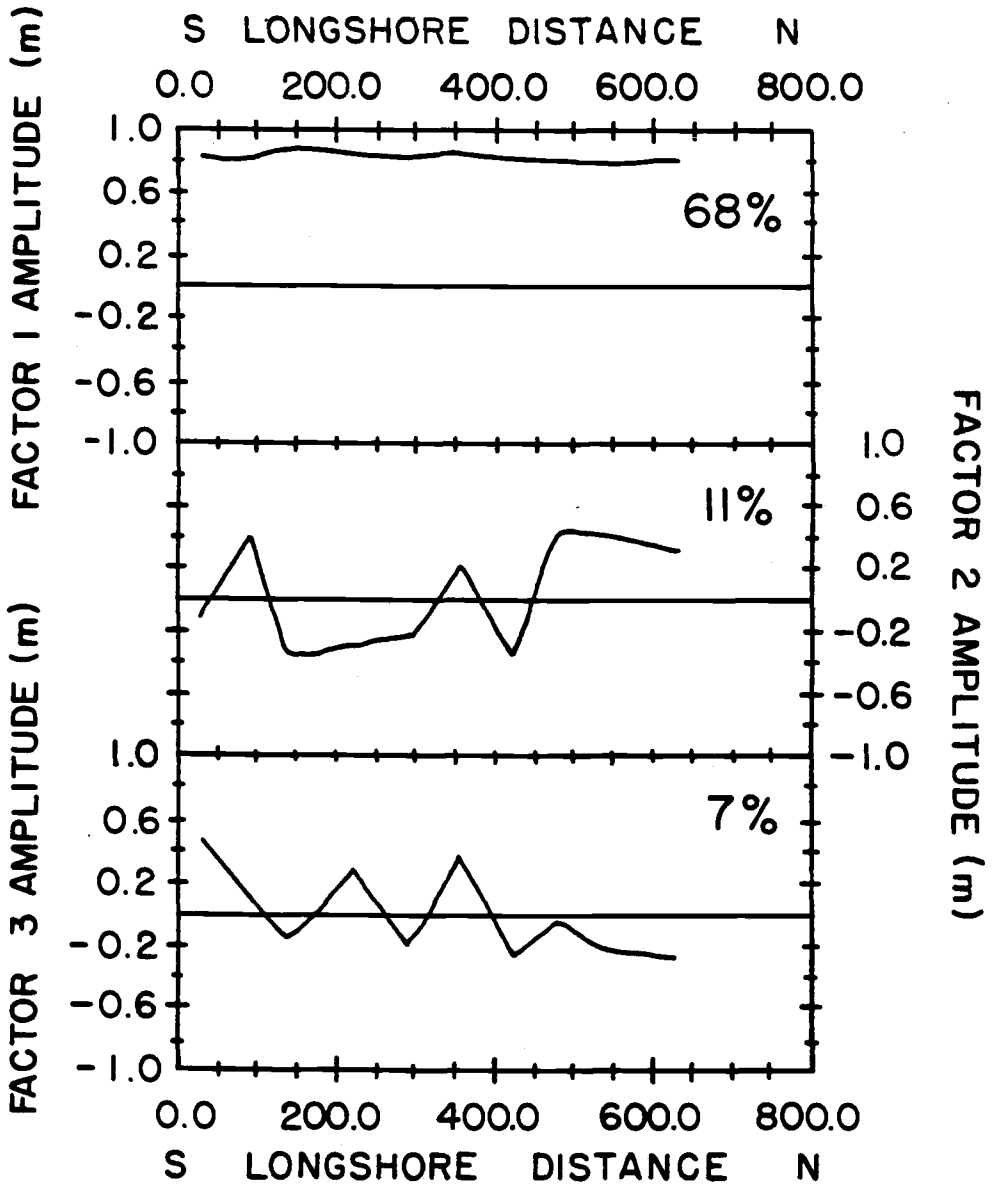

Figure 11. R-Mode Factors 1-3 of the longshore runup pattern on Day 3, after time series were randomly scrambled among their actual transect positions. The percent of total variance contributed by each factor is included.

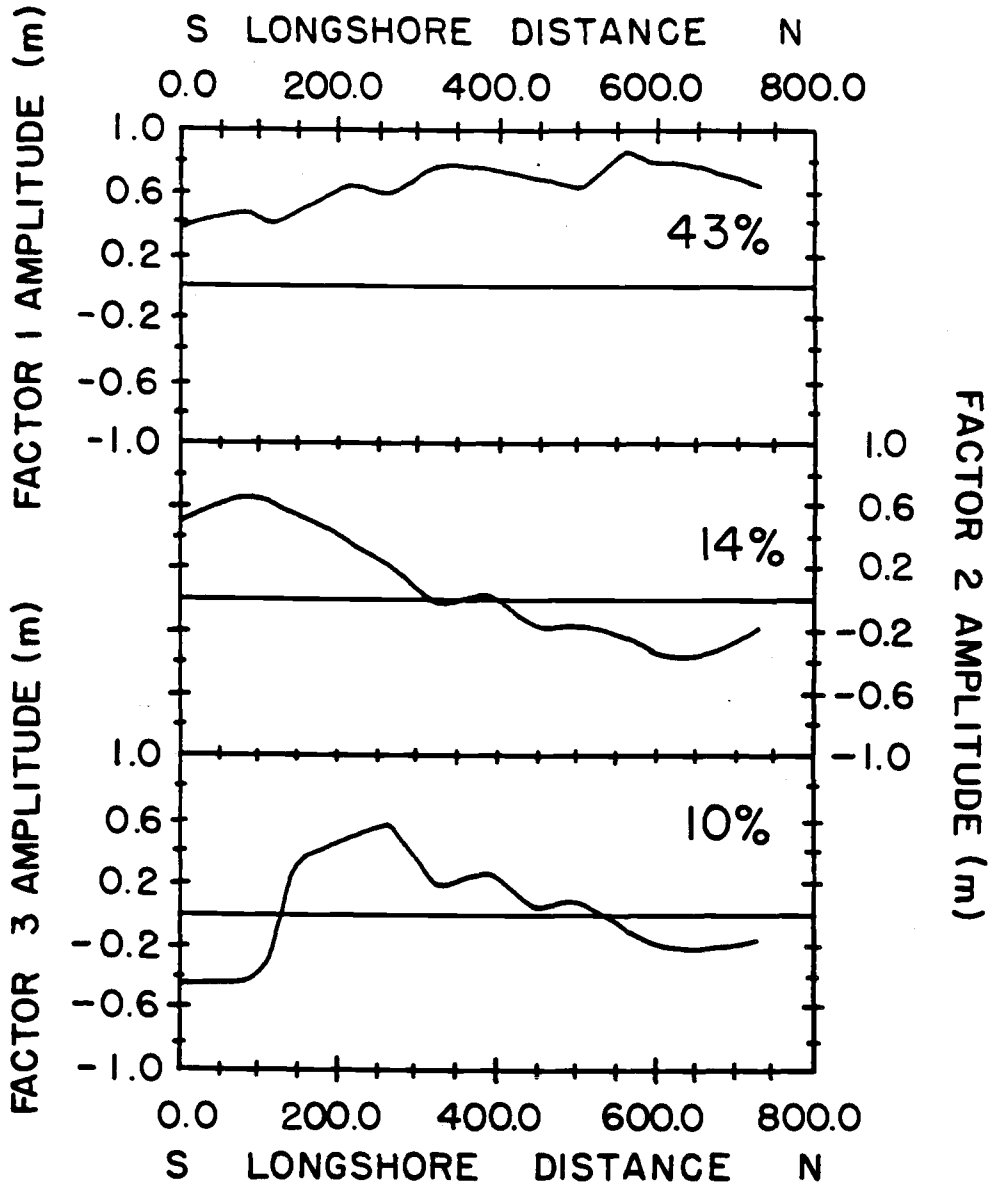

Figure 12. R-Mode Factors 1-3 of the longshore runup pattern on Day 1, with percent of total variance contributed by each factor.

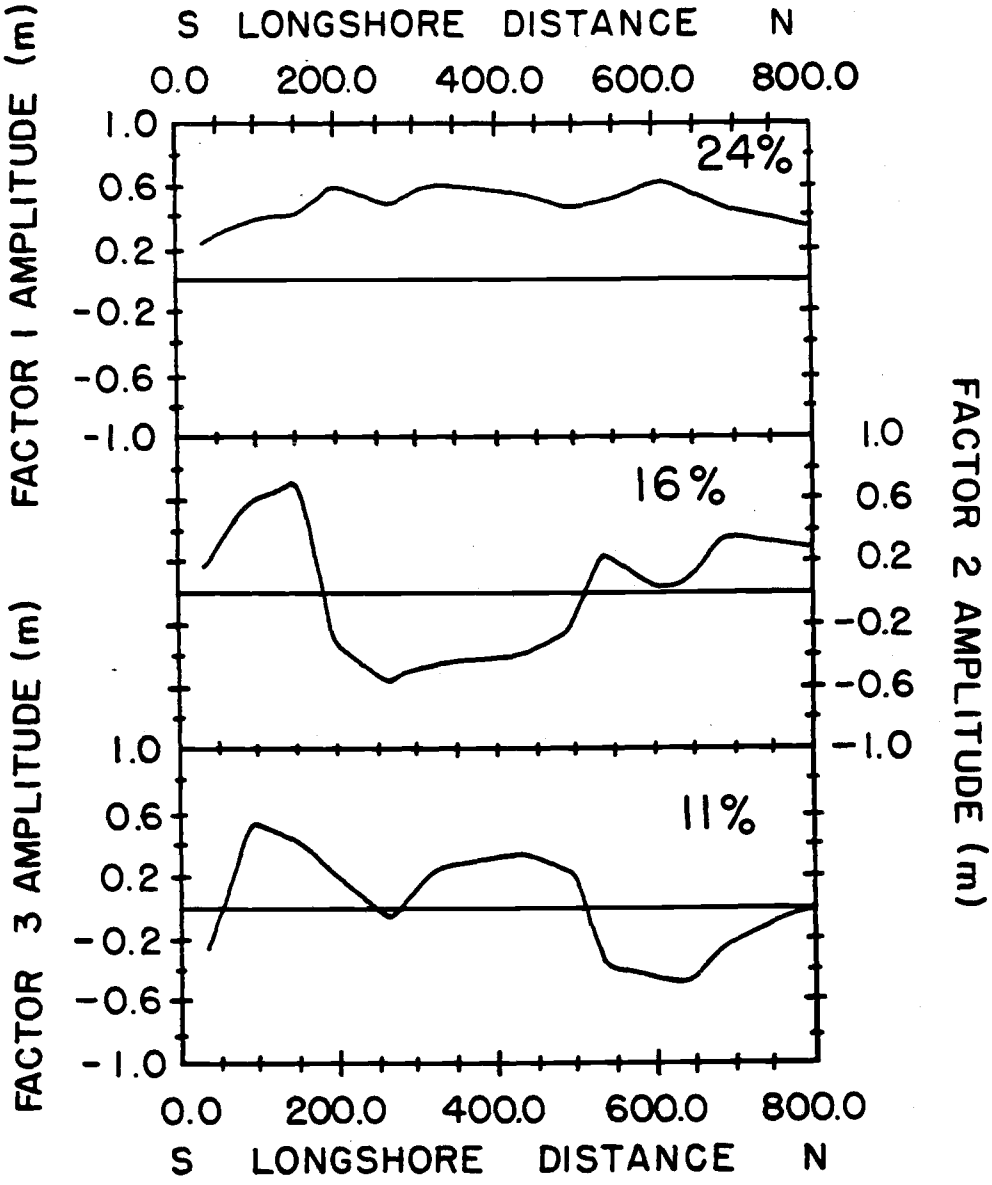

Figure 13. R-Mode Factors 1-3 of the longshore runup pattern on Day 2, with percent of total variance contributed by each factor.

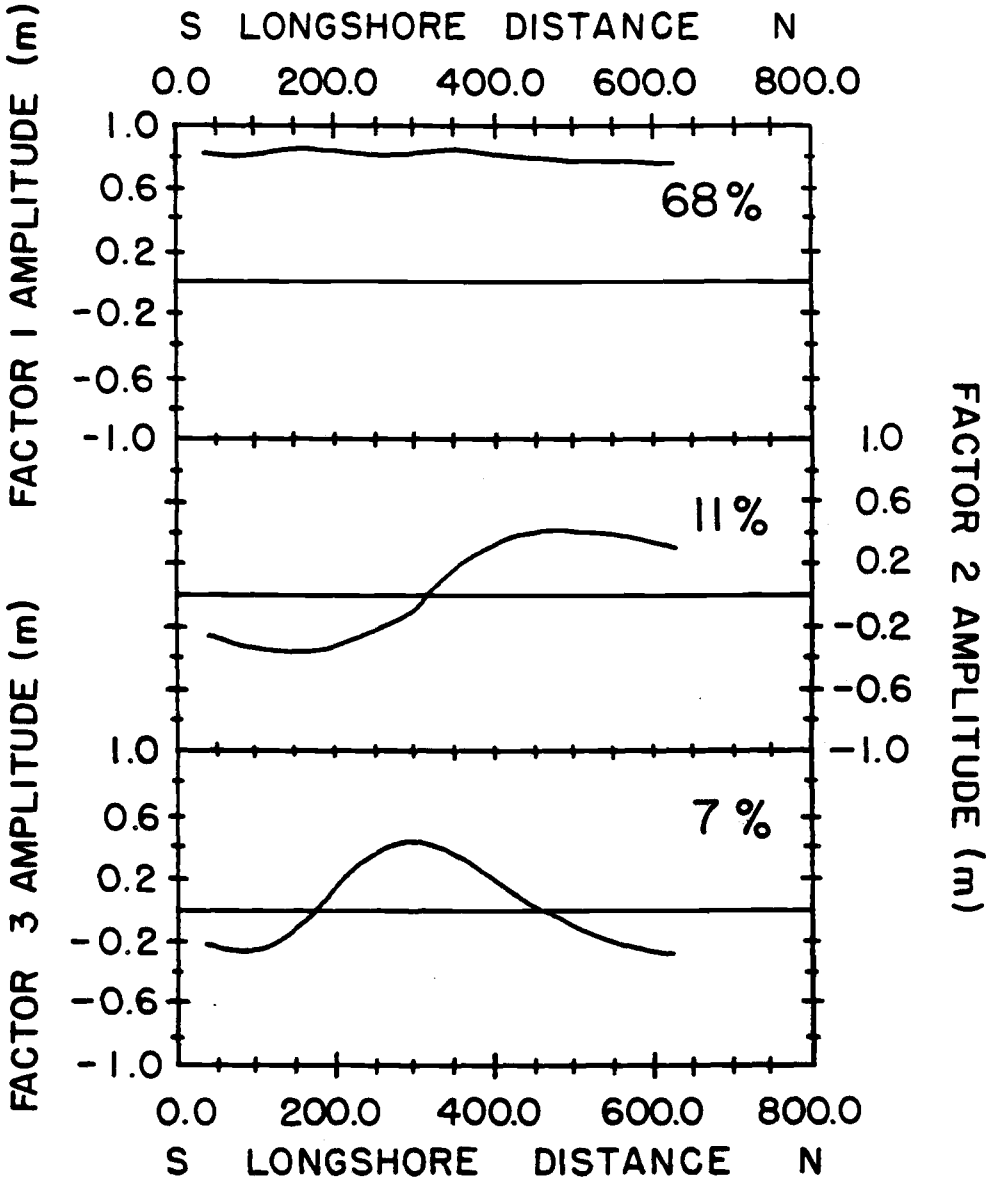

Figure 14. R-Mode Factors 1-3 of the longshore runup pattern on Day 3, with percent of total variance contributed by each factor.

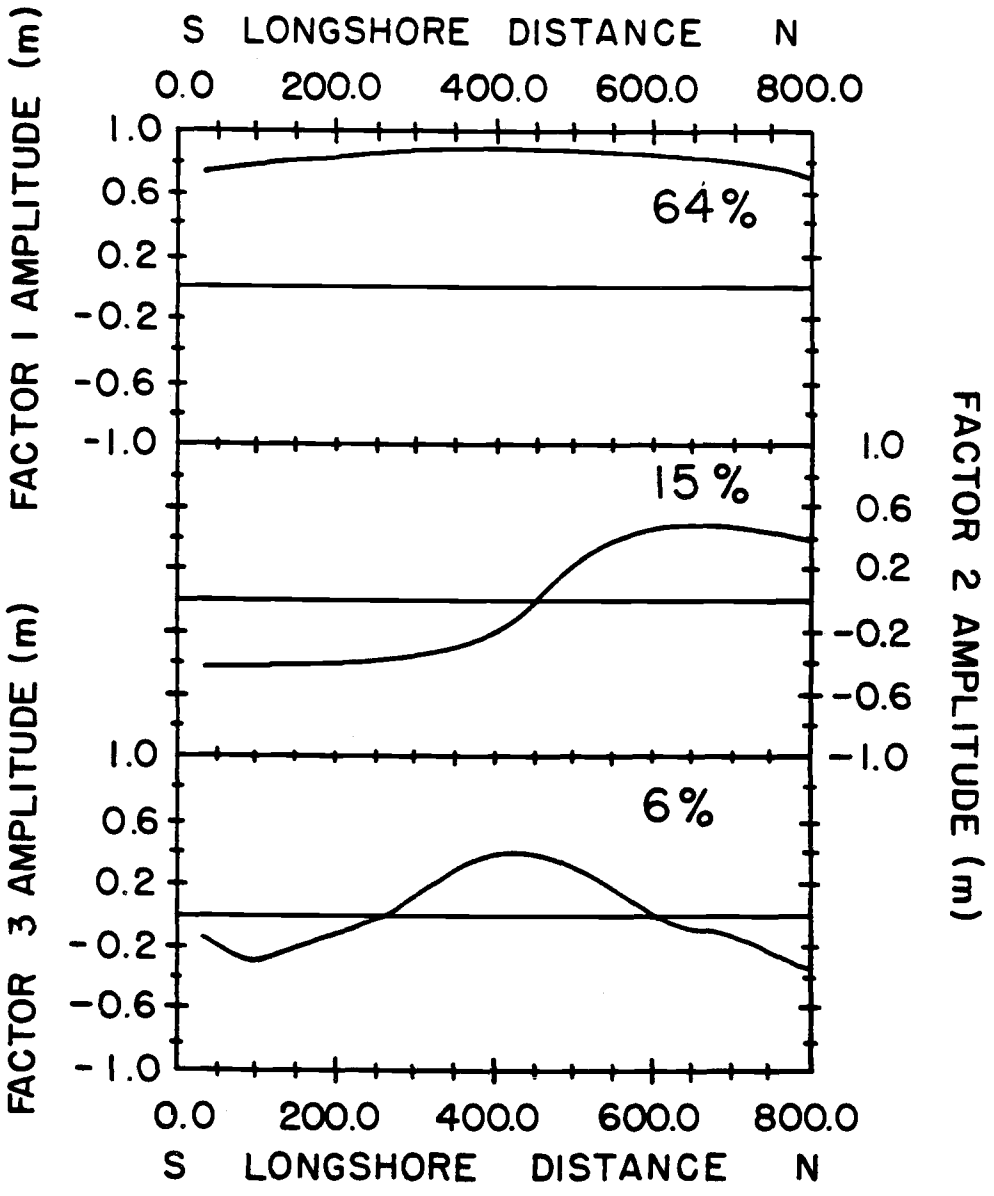

Figure 15. R-Mode Factors 1-3 of the longshore runup pattern on Day 4, with percent of total variance contributed by each factor.

when the variance explained is very low.

In Figures (12-15)a, Factor 1 is the single best covariance descriptor. Physically, this factor would "look" like the mean runup, and is an expression of the simple swash of the waves across the beach face [Davis, 1973]. The reconstructed Factor 1 time series for all data (not shown) follow the same slightly nonstationary trends as the corresponding original time series. The factor accounts for an equal amount of runup at all transects on each of Days 2, 3, and 4, and has a slight trend to the north for Day 1 that indicates differences in the complexity of the runup alongshore. The overall runup character alongshore was the least complicated on Day 3 and the most complicated on Day 2, as seen by the 68% and 24% of variance explained, respectively. The qualitative surf zone observations in Chapter 3 support this finding; on Day 2 the surf zone had the most diverse character alongshore, with short topographic and wave length scales.

The Factor Loadings for Factor 2 are shown in Figures (12-15)b. For Days 1, 3, and 4 a clear sinusoidal pattern is evident with one zero crossing at 400, 300, and 450 meters, respectively, and an evenly distributed amplitude about the zero crossing for Days 3 and 4. Day 2 does not fit this pattern, with 2 zero crossings at 175 and 525 meters, and an erratic amplitude distribution. The variances explained by Factor 2 for all data sets are comparable, ranging from 11-15%.

In Figures (12-15)c, Factor Loadings for Factor 3 follow a sinusoidal pattern for Days 3 and 4, with two zero crossings at 200 and 475 meters, and 250 and 600 meters, respectively. On Day

1 the pattern is skewed to the south and is slightly uneven, but resembles a sinusoid. Again, Day 2 looks quite different, with 4 zero crossings and no even pattern alongshore or about zero amplitude. The variances explained by Factor 3 range from 6-11%.

The longshore patterns of Factors 2 and 3 for Day 3 are off-center from the approximate longshore behavior expected for a standing edge wave. Data is also missing from the northern 2 transects on this day. To test the influence of the missing points, Factor Loadings were regenerated for Day 4 without the 3 southern transects. The resulting Factors 2 and 3 were slightly compressed alongshore and the entire pattern was shifted to the north (Figure 16). Evidently, the incomplete orthogonal mode gains an artificial nonzero mean, since variance is not equally distributed about the zero crossing (i.e. the mode appears slightly "leaky"). In order to regain the zero mean required by orthogonality, the decomposition compensates by shifting the zero crossings alongshore. From this test it was concluded that the Factor Loadings of Day 3 represent a shifted and compressed version of the real patterns. Note that leaky mode variance (Factor 1) may thus be an overestimate on Day 3, leaving Factors 2 and 3 minimum estimates of possible standing wave energy.

It is evident that Factors 2 and 3 for Days 1, 3, and 4 strongly reinforce the Fourier modeling technique presented in the last section. These factors could represent standing edge waves with longshore modes m=1,2, respectively, in the runup, whereas the erratic Day 2 factors do not. This discrepancy is not unexpected, in light of the difference in character between the

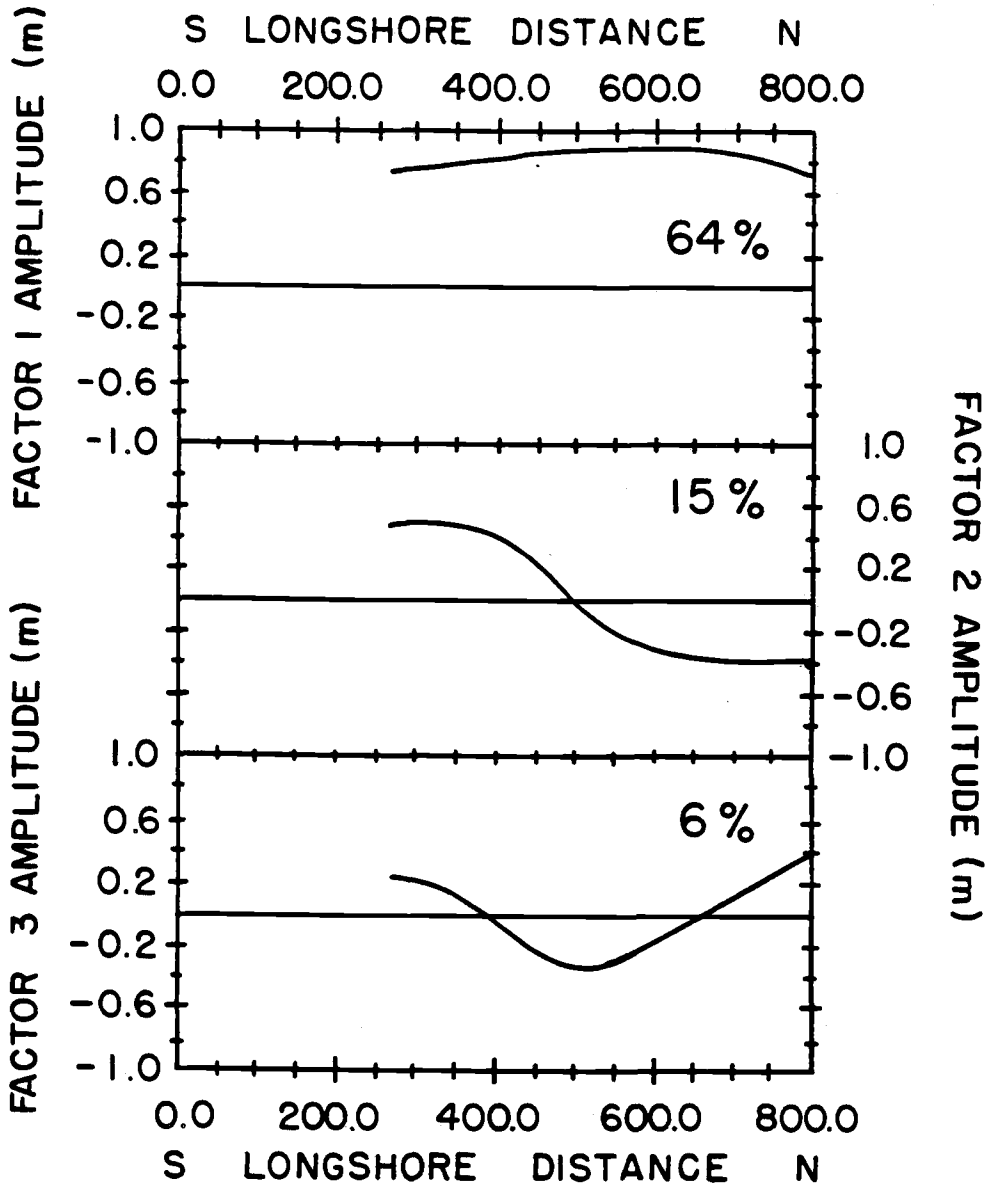

Figure 16. R-Mode Factors 1-3 of the longshore runup pattern on Day 4, using Transects E-M only in the decomposition. The percent of total variance contributed by each factor is included.

higher-energy, infragravity-dominated runup on Days 1, 3, and 4, and the low energy, higher-frequency runup on Day 2.

Spectral Analysis was applied to Factors 2 and 3 (Days 1, 3, and 4) to determine whether the energetic frequencies actually correspond to edge wave modes (m,n). The spectra (to .02Hz) are presented in Figure 17, with modes (m,n) marked by bands, identical to Figure 9.

The spectra for R-Mode Factors 2 and 3 are very similiar to the approximated Fourier modes (m=1,2) for Days 1, 3, and 4. A close agreement between Figure 17a (Factor 2) and Figure 9a (m=1) is immediately clear. The frequency distribution of variance is essentially identical for these two representations of an m=1 standing edge wave. In Figure 17b (Factor 3), the spectrum for Day 1 has a peak at .009Hz, whereas Figure 9b has energy split between .008Hz and .011Hz. Due to this shift in variance, mode (m,n)=(2,1) falls on an energy valley for the R-Mode decomposition, but crosses a peak for the Fourier mode. Peaks on Days 3 and 4 in Figure 17a are sharper than in Figure 9a, while retaining the same distribution.

Note that in all cases the Fourier modes have variances that are lower than the R-Mode variances. This is a reflection of the inaccurate sinusoidal approximation discussed in 5.1. The "shifting energy" of Day 1 (Figures 9b and 17b) is a result of the same simplified model. Random variance was extracted by the Fourier model (13) that was not accounted for by the similiar, but more realistic R-Mode Factor 3.

In the last section of this chapter, orthogonal factors in

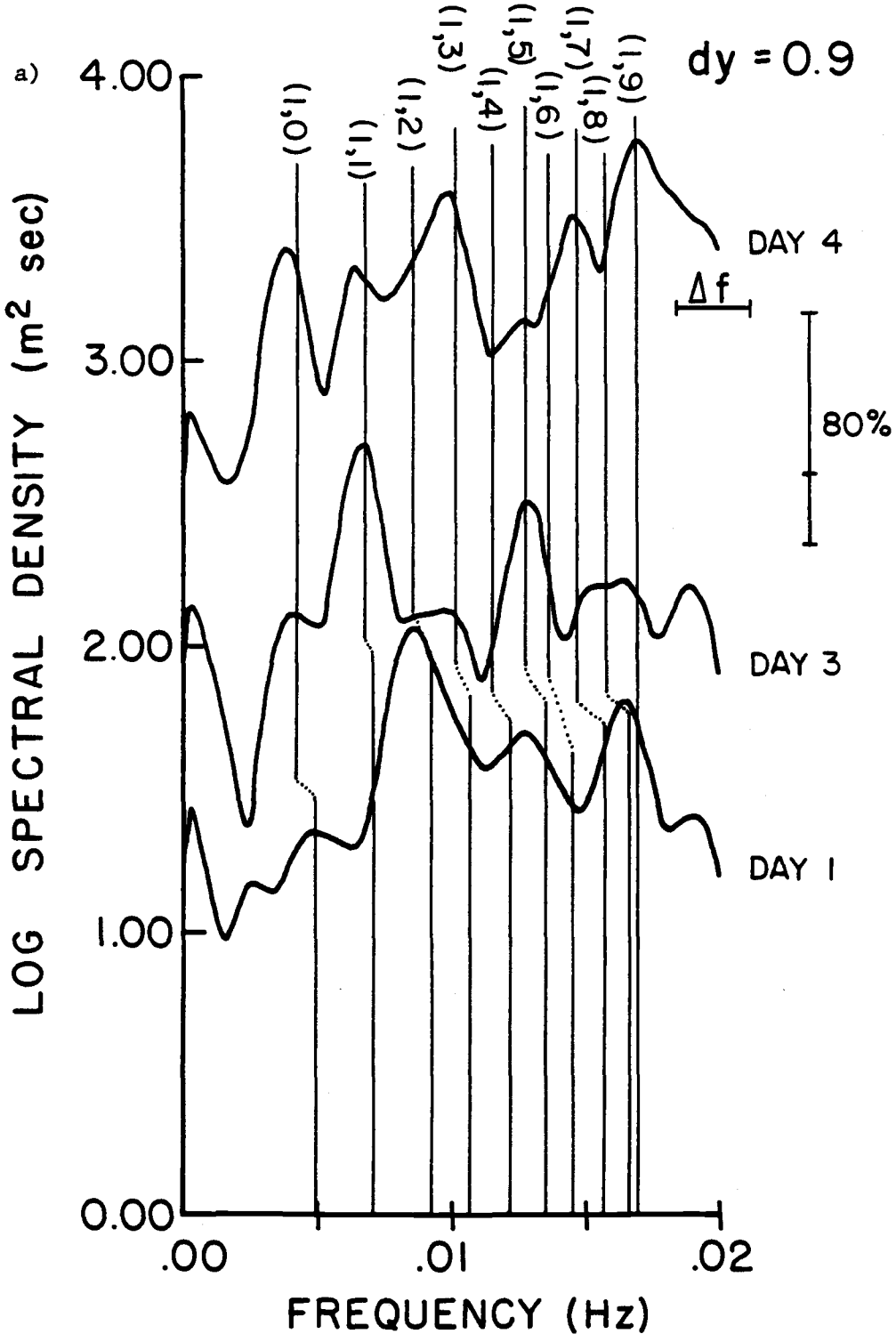

Figure 17. Spectra of runup for R-Mode Factors a) #2, and b) #3. Bands mark frequencies satisfying the edge wave dispersion relation for a) modes (m,n)=(1,n) and b) modes (m,n)=(2,n).

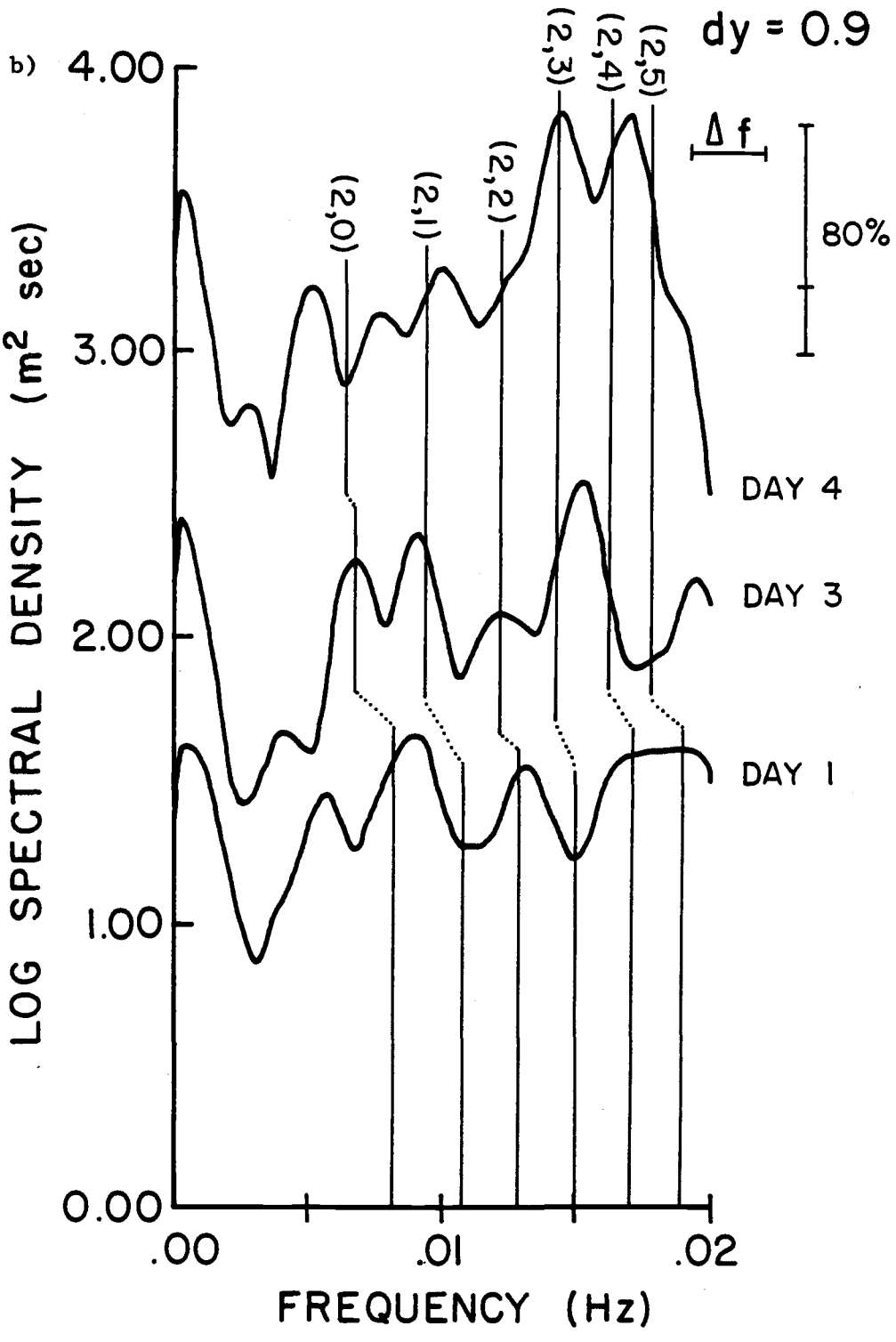

Figure 17 (continued).

the runup will be objectively determined while retaining frequency information as well. This introduces a very stringent criteria for satisfaction of the theoretical dispersion relation for possible longshore modes, m, that are revealed by the factors.

5.3 Complex Empirical Orthogonal Functions

Complex Empirical Orthogonal Function (EOF) Analysis is a principal components technique in the frequency domain. It is used here to more precisely examine the standing edge wave model by constraining the factors in frequency and computing their relative contribution to the total energy in a given band. It has been used successfully in similiar applications by Holman & Bowen [1984] and Romea and Smith [1983]. As in R-Mode Analysis, complex EOF Analysis empirically extracts the principal components of runup from the sample observations. The factors are linear combinations of the correlated elements of the cross-spectral matrix, U, of complex Fourier amplitudes from the N discretely sampled time series (10). The matrix elements are

$$U_{lj}(f) = C_{lj}(f) + iQ_{lj}(f) \; ; \quad (lj=1,\ldots,N) \qquad (17)$$

where $C_{lj}(f)$ and $Q_{lj}(f)$ measure the covariance of real (in-phase) and complex (out-of-phase) components, respectively, between transects l and j for a given frequency [Wallace & Dickenson, 1972].

As with R-Mode factors, the Factor Loading amplitudes

alongshore are the normalized eigenvector elements and the percent variance explained by a factor is equal to the ratio of its eigenvalue to the trace of U. The phase signature of a factor is obtained as

$$\theta_{1j}(f) = \tan^{-1}\left[-\frac{Q_{1j}(f)}{C_{1j}(f)}\right] \qquad (18)$$

Phase varies between $\pm 180^{0}$ and indicates the relative time lag of runup from one transect to another for a factor.

EOF factors have been computed for all data sets. Narrow bands of .002Hz width (9 degrees of freedom) were chosen to isolate the frequency of the factors as closely as possible. Particular interest is centered on infragravity frequencies (.003Hz-.02Hz) that could compliment the results from the two previous sections to satisfy the dispersion relation for infragravity edge wave modes (Figure 3; (8)).

The salient EOF results are summarized in Table III. Several possible modes (m,n) were revealed at different frequencies on each of the three days. The best-fit beach slope, $\hat{\beta}$, was chosen so that the edge wave frequency would be the central value of the .002Hz band (f-band). This was the most objective means of estimating a single value for both f and $\hat{\beta}$. The ratio $\hat{\beta}/\beta_e$ was computed for each mode and appears in the table. In accordance with theory, the resultant $\hat{\beta}$ values decrease with increasing mode n, in all but one case ((m,n)=(2,0), Day 4). Also included in Table III is the EOF Factor # (EOF#),

TABLE III

Standing edge wave mode (m,n) results from complex EOF analysis for Days 1, 3, and 4. All entries are defined in the text of Chapter V.

Day	f-band(Hz)	$\hat{\beta}$	$\frac{\hat{\beta}}{\beta_e}$	f	m	n	EOF#	$\%\sigma_T^2$(band)	a_e(cm)	$\%\sigma_T^2$(ig)
1	.006-.008	.017	1.00	.007	1	1	2	14	4.3	4.6
1	.012-.014	.016	0.94	.013	1	5	2	18	2.3	1.3
1	.008-.010	.040	1.14	.009	2	0	3	6	1.8	0.7
1	.013-.015	.020	1.17	.014	2	2	3	9	3.0	2.2
3	.005-.007	.013	0.87	.006	1	1	1	56	10.3	4.5
3	.016-.018	.015	1.00	.017	1	9	2	23	4.3	0.7
3	.008-.010	.014	0.93	.009	2	1	3	12	4.3	1.0
4	.003-.005	.017	0.94	.004	1	0	2	16	10.3	1.8
4	.008-.010	.017	1.13	.009	1	2	2	26	8.8	1.4
4	.012-.014	.016	1.07	.013	1	5	2	21	7.7	1.1
4	.016-.018	.015	1.00	.017	1	9	2	15	8.0	1.0
4	.004-.006	.013	0.62	.005	2	0	3	6	4.1	0.3
4	.013-.015	.014	0.93	.014	2	3	2	26	11.7	2.5

shoreline edge wave amplitude (a_e), and percent variance contribution by mode (m,n) to the .002Hz band ($\%\sigma_T^2$(band)) and to the infragravity (f<.05Hz) band ($\%\sigma_T^2$(ig)).

The full results are presented in Appendix 2 (Figures A2.1-A2.3) as plots of EOF Factor amplitude and phase alongshore. There is no expression of longshore standing motions for Day 2 from EOF's computed at bands out to .07Hz.

A typical set of EOF amplitude/phase results from one frequency band (.003Hz-.005Hz) decomposition is shown in Figure 18 for Day 4. EOF #1 explains 72% of the total variance in this band and has a constant amplitude and phase signature alongshore. It represents the motion of an infragravity leaky ($\sigma^2>g\lambda$) mode standing against the shoreline, reflecting untrapped energy back offshore. Other leaky mode energy emerged in several of the EOF's on Days 1, 3, and 4, accounting for at least 40% of the variance in the bands.

For the next EOF (#2; 16% of the band variance), the phase of the runup is close to 180° at the southern transects, goes through one clear 180° phase shift at 450 meters, and then remains at 0° to the northern headland. The amplitude pattern has antinodes at the headlands and one node corresponding to the phase shift position. This is the signature of a mode m=1 standing edge wave in the runup. From (8), the mode, n, is determined to be 0.

The shoreline amplitudes (a_e) of the standing edge waves were estimated from the runup variance (σ_T^2) in the EOF factors. Assuming that EOF #2 on Day 4 is composed entirely of edge wave mode (m,n)=(1,0) energy, a_e=10.3 cm (Table III).

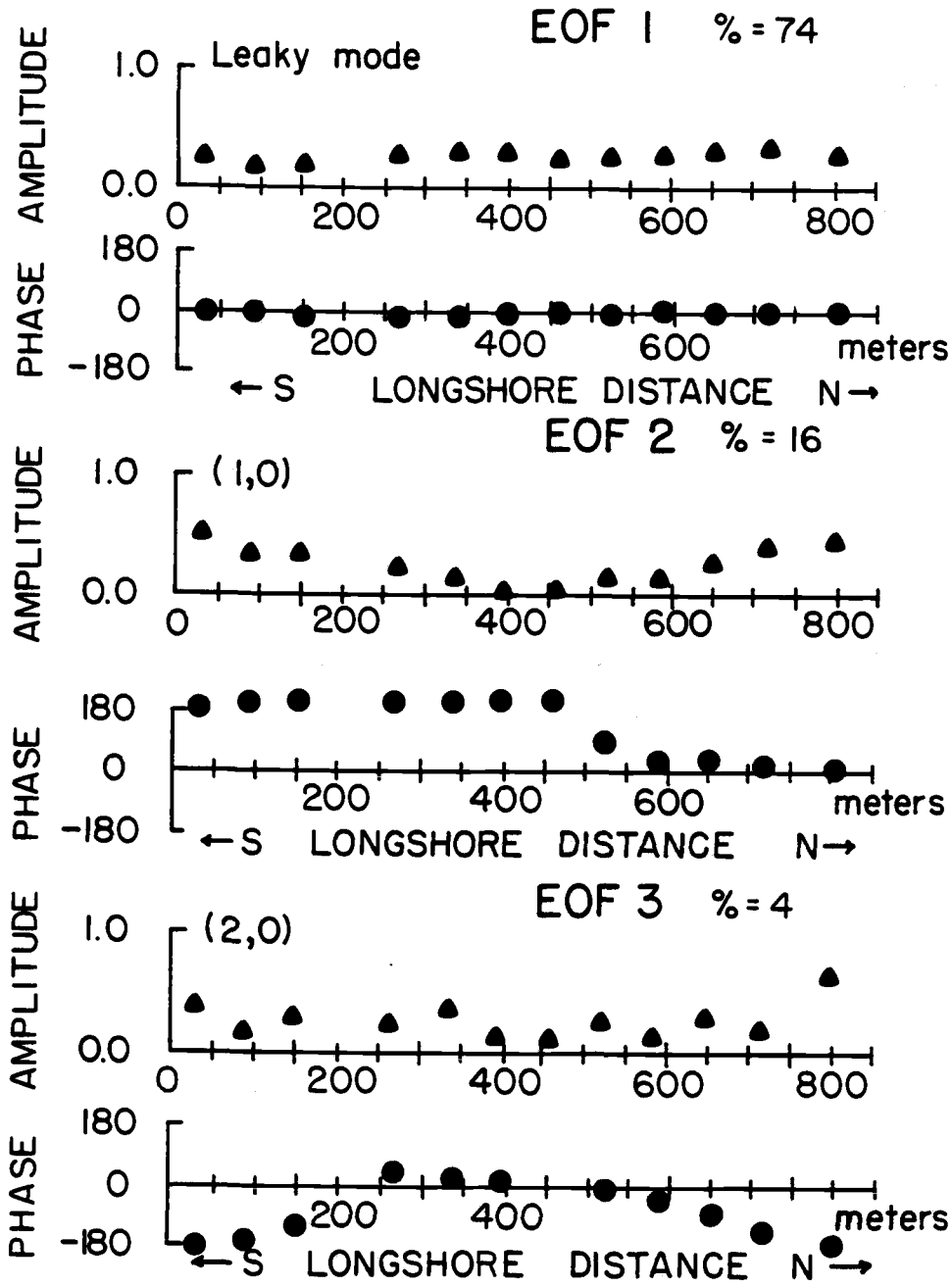

Figure 18. The amplitude/phase results for the frequency band .003Hz-.005Hz from complex EOF decomposition of the longshore runup signal on Day 4.

EOF #3 (6% of the band variance) has two less dramatic, but roughly equispaced phase shifts between 0^0 and 180^0 with an amplitude pattern that shows antinode-node character. Possible nodes at 200 meters and 550 meters correspond well to phase changes at those positions. The expression of a mode m=2 standing edge wave is strongly suggested (n=0 from (8)). Also supporting this interpretation is the close agreement of the amplitude patterns of EOF's #2 and #3 with the same R-Mode Factor Loadings #2 and #3 on this day (Figure 14). The amplitude, a_e, of this mode is estimated at 3.0 cm.

The other EOF's from Days 1, 3, and 4 in Appendix 2 reveal similiar phase/amplitude behavior and correspondence to the R-Mode factors. The mode (m,n)=(1,1) on Day 3 contributed the greatest portion of variance to any band, accounting for 56% of the runup variance at .005Hz-.007Hz. The single largest standing edge wave detected by the analysis was a mode (m,n)=(2,3) on Day 4. It explained 26% of the variance in the band .003Hz-.005Hz, had an amplitude of 11.7 cm, and accounted for 2.5% of the infragravity band runup variance on this day (Table III). Small differences in the EOF amplitude patterns from the sinusoidal model in some cases (Figures 2 and 8) reflect a longshore behavior (f(y,t)) that is not exactly sinusoidal for standing edge waves on this beach. This is a result of the nonplanar longshore profile (3b).

In a special case, EOF modes (m,n)=(1,1) on Day 1 (a_e=4.3 cm) and (m,n)=(1,2) on Day 4 (a_e=8.8 cm) both have strong phase signatures of an m=1 standing edge wave with one sharp 180^0 transition at mid-beach (Figures A2.1 and A2.3). However, the

amplitude patterns for these EOF's have an extra node at about 250 meters that does not fit the m=1 model. The probable explanation is that the rip current located at 250 meters on these days altered the edge wave behavior, diminishing its height and runup amplitude in this area. During the experiments all local wave activity was visibly undercut by this seaward-moving current.

Comparison of Table III to the R-Mode and Fourier mode spectra (Figures 9 and 17) discloses some remarkable agreements between the results of the three techniques. The restricting frequency information of the EOF Analysis lends confidence to the broad peaks of the R-Mode spectra. In many instances, the EOF results match very well to the spectral peaks. For instance, on Day 3 EOF mode (m,n)=(1,1) is centered at .006Hz, matching an R-Mode Factor 2 peak in Figure 17a, and EOF mode (m,n)=(2,0) (Day 1) agrees with a peak at .008Hz in Figure 17b.

The $\hat{\beta}/\beta_e$ values in Table III show that the $\hat{\beta}$ values obtained from the complex EOF results are very close to the estimated effective slope β_e (Table II), although discrepancies do occur. For instance, for (m,n)=(2,0) on Day 1, $\hat{\beta}$ (.040) is steeper than β_e (.035), suggesting that for this mode the slope affecting the edge wave may be slightly greater (weighted more toward the shore) than predicted by the β_e model of Holman and Bowen [1979]. However, this slope difference disappears if the actual edge wave frequency is .0083Hz instead of the central value (.009Hz) of the .002Hz band (Table III). For all modes (m,n), differences between β_e and $\hat{\beta}$ can be resolved similiarly.

The relative accuracy of the two slope estimates may be

determined by comparing the frequencies of the R-Mode spectral peaks in Figure 17 to the edge wave mode frequencies obtained using each estimate, $\hat{\beta}$ (EOF result) and β_e (bands on spectra). There is close agreement between the two models and exact correspondence in one case ((m,n)=(1,1)). The complex EOF results (Table III) do not indicate consistently higher or lower frequencies than the (m,n) bands of the β_e model. However, in almost every case the complex EOF frequency results match the central frequency of the R-Mode spectral peaks better than the (m,n) bands. On Day 4 for example, EOF modes (m,n)=(1,0), (1,2), and (2,0) correspond much better to peaks than the (m,n) bands for the same modes.

CHAPTER VI
DISCUSSION

The aspect ratio $\tilde{L}=L_y/L_x$ was used to investigate why the standing edge waves in Table III may appear on Short Sands Beach, and why certain modes dominate, as seen by the relative amounts of variance contributed to the runup. To check the reasonableness of the modes, $\tilde{L}$ was computed for each mode (m,n), similiar to the nondimensional ratio between edge wave offshore length scale and surf zone width computed by Bowen and Inman [1969]. This ratio between longshore wavelength (L_y) and offshore length scale (L_x) should be constant for a given mode, n, where

$$\tilde{L} = \frac{2\pi g(2n+1)\hat{\beta}}{L_x \sigma^2} \qquad (19)$$

from the theoretical dispersion relation (6), and $2\pi g\hat{\beta}/2\pi$ is constant for a particular experiment. In this study L_y has only two possibilities, 1600 meters when m=1 and 800 meters when m=2.

In Figure 19, the cumulative offshore energy function is plotted for edge wave modes n=0-3. This figure was used to determine L_x as follows: χ was read from Figure 19 at 95% of the cumulative offshore energy for each mode n. From this χ value, L_x was computed for each mode (m,n) using the $\hat{\beta}$ and f values in Table III. In Table IV, $L_x(95\%)$, $\tilde{L}$, and %E (the percent of

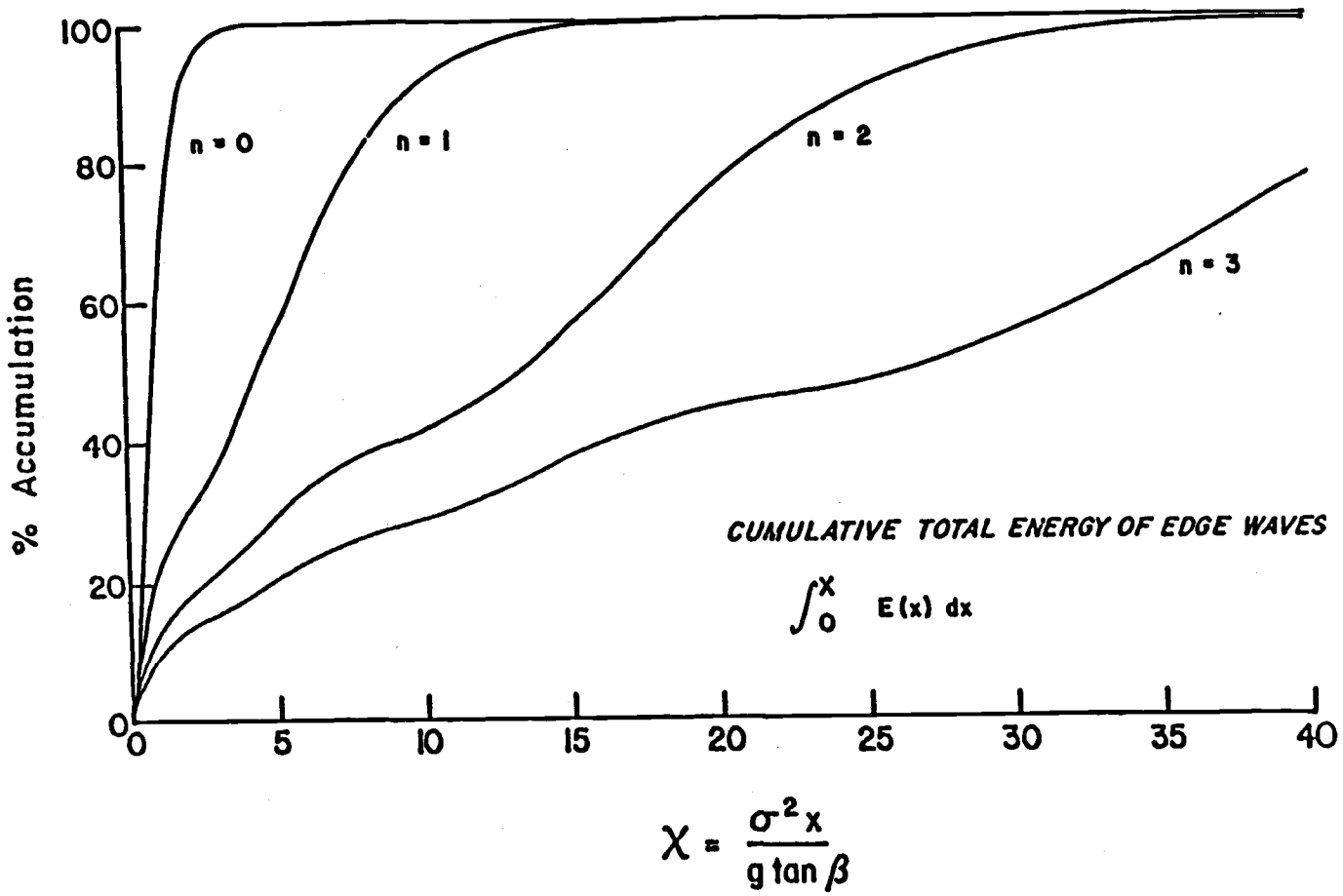

Figure 19. The cumulative percent of energy for edge wave modes 0-3 as a function of non-dimensional offshore distance χ.

total edge wave mode (m,n) energy contained within the headlands, x=800m) are listed for each mode (m,n), along with the percent variance contributed to the infragravity band ($\%\sigma_T^2$(ig)). For n=5 and n=9, the $\tilde{L}$ and L_x values are ball-park estimates.

The results show little difference in $\tilde{L}$ for each mode, n, and some of the variation is due to differences in the individual beach slope ($\hat{\beta}$) affecting the different modes. $\tilde{L}$ also decreases for increasing n as expected. Physically, this means that as n increases the edge wave form "stretches" out across shore relative to its longshore length, so that for larger n, a greater portion of the edge wave energy is away from the shore and the surf zone. Also, for a given n, edge waves with smaller longshore modes, m, (i.e. longer L_y) must extend further offshore to maintain the constant ratio $\tilde{L}$.

Earlier investigations [Bowen and Inman, 1969] demonstrated that laboratory surf zone turbulence has a significant damping effect on edge waves. Therefore, modes that extend further beyond the breaking waves on a real beach are expected to dominate the edge wave field. However, another important consideration is the offshore extent of the headlands, since standing wave energy is "held" in the cove by these reflectors. Modes with a large percent of total energy extending offshore beyond the headlands are not expected to stand in the cove, since large amounts of energy would constantly escape around the headlands and progress alongshore.

In Table IV, the complex EOF results show that in every case, mode m=1 dominates over mode m=2 for each mode n,

TABLE IV

Descriptive properties of edge wave modes (m,n) for Days 1, 3, and 4. Included are offshore length scale (L_x(95%)), aspect ratio ($\tilde{L}$) between edge wave wavelength, L_y, and L_x, and the percent of total mode (m,n) energy contained within the headlands of the cove (%E). $\%\sigma_T^2$(ig) reappears from Table III.

Day	mode(m,n)	Lx(95%)(m)	$\tilde{L}$	%E	$\%\sigma_T^2$(ig)
4	(1,0)	395	4.20	100	1.8
1	(2,0)	185	4.15	100	0.5
4	(2,0)	195	4.15	100	0.3
1	(1,1)	860	1.89	89	4.6
3	(1,1)	895	1.89	88	4.5
3	(2,1)	430	1.88	100	1.0
4	(1,2)	1,260	1.29	50	1.4
1	(2,2)	630	1.26	100	2.2
4	(2,3)	915	0.89	93	2.5
1	(1,5)	2,000+	0.80	<50	1.3
4	(1,5)	2,000+	0.80	<50	1.1
3	(1,9)	$0(10^3)$	?	<25	0.7
4	(1,9)	$0(10^3)$	?	<25	1.0

supporting the argument outlined above. For example, (m,n)=(1,1) and (2,1) on Day 3 contribute 4.5% and 1.0% of the variance in the infragravity band, respectively. Also, the fundamental mode n=0 which is contained the closest to the shore shows the lowest overall variance contributions to the runup. More specifically, the two modes (m,n)= (2,0) (Days 1 and 4) that have the lowest L_x values have the lowest observed $\%\sigma_T^2$(ig) values (0.5% and 0.3%). This supports the suggestion that higher modes extending further beyond the surf zone are less affected by turbulent damping, so that they "survive" preferentially.

These results are illustrated very clearly in Figure 20, where the $\%\sigma_T^2$(ig) values of each edge wave mode are plotted against their offshore lengths normalized by the length of the headlands ($L_x/L_{headlands}$).

An interesting observation can be made about the possible modes n=5 and n=9. The offshore extent of the energy is much greater than 800 meters for both modes (greater than 50% for n=5 and greater than 75% for n=9, from the %E values). However, the R-Mode spectra (Figure 17) and the complex EOF amplitude/phase results (Figures A2.1a and A2.3a) clearly indicate standing wave energy corresponding to the edge wave mode n=5 (f=.013Hz) on Days 1 and 4. Non-trivial amplitudes of 2.3 cm and 7.7 cm were estimated (Table III).

One possible explanation is that mode (m,n)=(1,5) actually is a high mode standing edge wave. This would imply a very strong edge wave forcing mechanism, adding at least as much energy to the mode as the amount lost alongshore over each edge

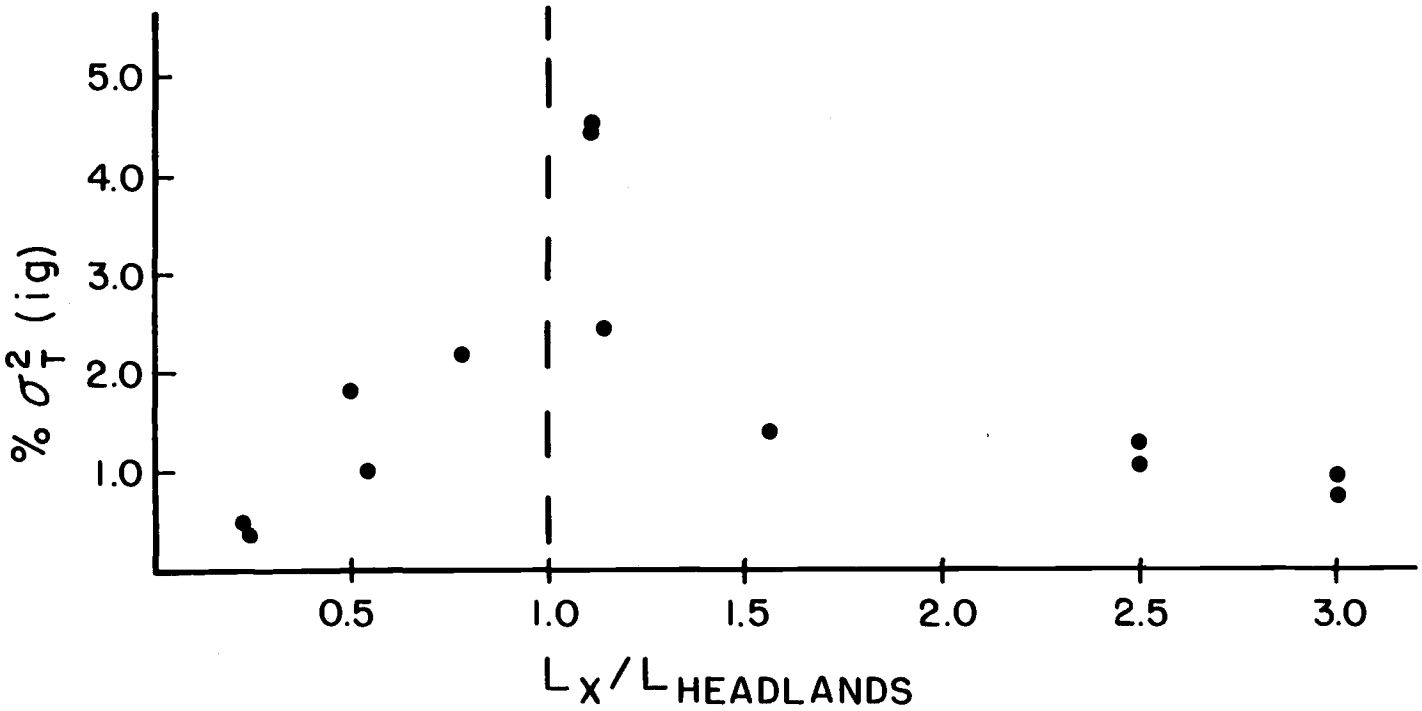

Figure 20. The variance contribution of the standing edge wave modes to the infragravity band ($\%\sigma_T^2$(ig)) as a function of the offshore edge wave length scale divided by the length of the headlands ($L_x/L_{Headlands}$).

wave period. For mode n=5 this would require a renewing of at least 50% of the energy about every 70 seconds (Table IV) on this beach. It is unlikely that the forcing mechanism is this efficient.

Another possibility is that this mode represents a small amount of energy in the landward tail of a larger, coastally trapped wave on the continental shelf that extends into the cove and remains trapped there between the headlands. This standing wave energy would have a constant energy input from the shelf wave.

For the mode n=9 Figure 17a has an energetic region near the theoretical edge wave frequency of .017Hz for Days 3 and 4. However, the complex EOF results on Day 3 show that the node and phase shifts for mode (m,n)=(1,9) are located at 250 meters instead of mid-beach, as they are for mode (m,n)=(1,0) on this day (Figure A2.2a). The mode n=9 probably has a longshore modal number less than m=1, and is standing inperfectly in the cove as leaky mode energy (i.e. $\sigma^2 > g\lambda$). On Day 4, the phase signature of (m,n)=(1,9) trends from 180° to 0° instead of passing through a sharp transition (Figure A2.3a). This also implies leakiness. Note that the $\%\sigma_T^2$(ig) values for this mode are small, but not insignificant.

Information about the strength of natural edge wave resonances is available in those R-Mode spectra representing the frequency distribution of variance in the m=1 (Figure 17a) and m=2 (Figure 17b) standing edge wave models. Spectral peaks that correspond to modes (m,n) revealed by the complex EOF results are

broad and detuned, indicating that the bounded beach system does not produce a well-tuned resonance.

For an edge wave forcing mechanism such as the model of Gallagher [1971] or Symonds et al. [1982], incoming incident wave trains transfer broad-banded energy to infragravity waves at the incident group frequency and length scales. As explained in Chapter 2, in the topographically bounded cove resonance is expected at a single frequency that compliments the closest mode (m,n) pair to satisfy the theoretical dispersion relation (8). This single frequency scenario assumes a perfectly resonating system, such as a well-tuned guitar that resonates to a single note from the broad spectrum of sound produced by plucking one string.

In Ursell's [1952] experiments with standing edge waves (see Chapters 1, 2) very sharp resonances did occur at frequencies satisfying (8). However, that study was conducted in a smooth, cement laboratory basin with exactly vertical side walls. For the Short Sands Beach system to be a perfect resonator, the headlands would have to be pure reflectors. The walls would have to be exactly vertical and smooth, preventing turbulence and dissipation from imperfect reflection.

This is not probable on a natural beach and is certainly not the case on Short Sands Beach where large rocks lay at the base of the headlands and the wall surfaces are irregular. On the real beach, broad-banded energy input to the system resonates imperfectly, narrowing about the standing edge wave frequency rather than to a single value, as seen in the R-Mode spectra

(Figure 17). This case can be compared to the guitar with a bridge made of soft cardboard instead of a piece of straight, hard wood. The notes will be out of tune, or weakly resonant.

CHAPTER VII
SUMMARY

The model for topographic trapping of infragravity edge waves has been substantiated on Short Sands Beach. The theoretical dispersion relation for standing edge waves (8) was satisfied by at least 9 modes (m,n), revealed by the complex EOF decomposition of the longshore runup signal on three different days. The R-Mode factor patterns and the spectral results of R-Mode and Fourier Analyses strongly support the EOF modes (m,n).

The wave runup spectra (Figure 7) from Days 1-4 on Short Sands Beach show that infragravity-band runup energy increased relative to incident band runup as deep water wave heights increased. On all three infragravity-dominated Days (1, 3, and 4), at least 95% of the runup variance was at frequencies less than .05Hz, with individual low mode ($m=1,2$; $n\leq 3$) standing edge waves contributing up to 4.6% of that energy.

The shoreline amplitudes of the standing edge waves range from 1.8 cm to 11.7 cm compared to the significant runup amplitudes of 30 cm, 57 cm, and 65 cm on Days 1, 3, and 4, respectively. While these shoreline amplitudes are small compared to incident band wave heights on this coast, they make up a significant portion of the total runup variance. The total standing edge wave variance in all modes accounted for 8.8%, 6.2%, and 8.1% of the total infragravity runup variance on Days 1, 3, and 4, respectively. In light of the relatively mild winter wave conditions represented on these days, the figures are impressive.

Much larger winter storm waves would pump considerably more variance into the infragravity band, and presumably into edge wave modes as seen in this study.

For all of the resulting modes (m,n), higher modes, n, have larger variances overall, and for a given mode, n, edge waves with the lower mode m=1 (larger longshore length, L_y) have larger variances than those with mode m=2. This dominance of modes (m,n) that extend further offshore indicates that turbulent surf zone damping is an important parameter in the edge wave dynamics on this dissipative beach. On the other hand, modes n=5 and n=9 are more likely to be leaky wave modes than edge waves, since at least 50% and 75% of the energy in these modes extends further offshore than the reflecting headlands that trap the energy.

From the breadth of mode (m,n) combinations represented in this study, it is clear that infragravity energy at a wide range of frequency and length scales is successfully trapped and "filtered" by the reflecting headlands. However, the natural resonances of standing edge waves are not sharp on this beach. This is readily apparent in the broad, detuned peaks of the R-Mode and Fourier spectra. It would be difficult to quantitatively assess the strength of the resonance the broadly forced energy does undergo without having a better handle on the mechanism and scale of energy transfer from the incident wave groups.

REFERENCES

Aubrey, D.G. (1980). Our dynamic coastline. Oceanus, 23(4), pp. 4-14.

Ball, F.K. (1967). Edge waves in an ocean of finite depth. Deep Sea Research, 14, pp. 79-88.

Bowen, A.J. (1972). Edge waves and the littoral environment. Proceedings of the 13th Coastal Engineering Conference, ASCE, pp. 1313-1320.

Bowen, A.J. (1980). Simple models of nearshore sedimentation; beach profiles and longshore bars, in The Coastline of Canada, edited by S.B. McCann. Geological Survey of Canada, Ottawa, pp. 1-11.

Bowen, A.J. and R.T. Guza (1978). Edge waves and surf beat. Journal of Geophysical Research, 83, pp. 1913-1920.

Bowen, A.J. and D.L. Inman (1969). Rip currents, 2, Laboratory and field observations. Journal of Geophysical Research, 74(23), pp. 5479-5489.

Bowen, A.J. and D.L. Inman (1971). Edge waves and crescentic bars. Journal of Geophysical Research, 76(36), pp. 8662-8670.

Creech, C. (1981). Nearshore wave climatology, Yaquina Bay, Oregon. Sea Grant College Program, ORESU-T-81-002.

Davis, J.C. (1973). Statistics and Data Analysis in Geology. John Wiley and Sons, New York, NY, 550 p.

Davis, R.E. (1976). Predictability of sea surface temperature and sea level pressure anomalies over the North Pacific Ocean. Journal of Physical Oceanography, 6, pp. 249-266.

Dolan, R., B. Hayden and W. Felder (1979). Shoreline periodicities and edge waves. Journal of Geology, 87, pp. 175-185.

Eckart, C. (1951). Surface waves in water of variable depth. Lecture Notes, Fall Semester 1950-1951, Marine Physical Laboratory of the Scripps Institute of Oceanography. Wave Report No. 100, SIO Reference 51-12 (Unpublished manuscript), 99 p.

Gallagher, B. (1971). Generation of surf beat by non-linear wave interactions. Journal of Fluid Mechanics, 49, pp. 1-20.

Galvin, C.J. (1965). Resonant edge waves on laboratory beaches. Transactions of the American Geophysical Union (abstract), 46, p. 112.

Guza, R.T and A.J. Bowen (1976). Resonant interactions for waves breaking on a beach. Proceedings of the 15th Coastal Engineering Conference, ASCE, pp. 560-579.

Guza, R.T. and R.E. Davis (1974). Excitation of edge waves by waves incident on a beach. Journal of Geophysical Research, 79(9), pp. 1285-1291.

Guza, R.T. and D.I. Inman (1975). Edge waves and beach cusps. Journal of Geophysical Research, 80(21), pp. 2997-3012.

Guza, R.T. and E.B. Thornton (1982). Swash oscillations on a natural beach. Journal of Geophysical Research, 87, pp. 483-491.

Holman, R.A. (1981). Infragravity energy in the surf zone. Journal of Geophysical Research, 86(C7), pp. 6442-6450.

Holman, R.A. and A.J. Bowen (1979). Edge waves on complex beach profiles. Journal of Geophysical Research, 84(C10), pp. 6339-6346.

Holman, R.A. and A.J. Bowen (1982). Bars, bumps, and holes: Models for the generation of complex beach topography. Journal of Geophysical Research, 87(C1), pp. 457-468.

Holman, R.A. and A.J. Bowen (1984). Longshore structure of infragravity wave motions. Journal of Geophysical Research, 89(C4), pp. 6446-6452.

Holman, R.A. and R.T. Guza (1984). Measuring run-up on a natural beach. Coastal Engineering, 8, pp. 129-140.

Holman, R.A. and A.H. Sallenger (1984). Longshore variability of wave run-up on natural beaches. Proceedings of the 19th Coastal Engineering Conference, ASCE, pp. 1896-1912.

Huntley, D.A. (1976). Long-period waves on a natural beach. Journal of Geophysical Research, 81(36), pp. 6441-6449.

Huntley, D.A., R.T. Guza and E.B. Thornton (1981). Field observations of surf beat, 1, Progressive edge waves. Journal of Geophysical Research, 86(C7), pp. 6451-6466.

Jenkins, G.M. and D.G. Watts (1968). Spectral Analysis and its Applications. Holden-Day, Oakland, CA, 525 p.

Kaplan, W. (1981). Advanced Mathematics for Engineers, Addison-Wesley, Reading, Mass., 929 p.

Katoh, K. (1981). Analysis of edge waves by means of empirical eigenfunctions. Report of the Harbor Institute 20, pp. 3-51.

Komar, P.D. (1973). Observations of beach cusps at Mono Lake, California. Geological Society of America Bulletin, 84, pp. 3593-3600.

Longuet-Higgins, M.S. and R.W. Stewart (1964). Radiation stress in water waves; a physical discussion, with applications. Deep Sea Research, 11, pp. 529-562.

Munk, W.H. (1949). Surf beats. Transactions of the American Geophysical Union, 30(6), pp. 849-854.

Oltman-Shay, J. and R.T. Guza (in press). Infragravity edge wave observations on two California beaches. Journal of Geophysical Research.

Pearce, J.A. (1976). Statistical analysis of major element patterns in basalt. Journal of Petrology, 17(1).

Pisias, N.P. (1978). Paleoceanography of the Santa Barbara Basin during the last 8000 years. Quaternary Research, 10, pp. 366-384.

Romea, R.D. and R.L. Smith (1983). Further evidence for coastal trapped waves along the Peru Coast. Journal of Physical Oceanography, 13(8), pp. 1341-1356.

Sasaki, T., K. Horikawa and S. Hotta (1976). Nearshore current on a gently sloping beach. Coastal Engineering Japan, 18, pp. 123-142.

Stokes, G.G. (1846). Report of the British Association, Part 1, also 1880, Mathematical and Physical Papers (Collected), 1, pp. 92-100.

Symonds, G., D.A. Huntley and A.J. Bowen (1982). Two-dimensional surf beat: Long wave generation by a time-varying breakpoint. Journal of Geophysical Research, 87(C1), pp. 492-498.

Tucker, M.J. (1950). Surf beats: Sea waves of 1 to 5 minute period. Proceedings of the Royal Society, Series A, 202, pp. 565-573.

Ursell, F. (1952). Edge waves on a sloping beach. Proceedings of the Royal Society, Series A, 214, pp. 79-97.

Wallace, J.M. and R.E. Dickenson (1972). Empirical orthogonal representation of time series in the frequency domain, 1, Theoretical considerations. Journal of Applied Meteorology, 11, pp. 887-892.

Wright, L.D., J. Chappell, B.G. Thom, M.P. Bradshaw and P. Cowell (1979). Morphodynamics of reflective and dissipative beach and inshore systems, Southeastern Australia. Marine Geology, 32, pp. 105-140.

APPENDICES

APPENDIX 1:

WAVE RUNUP POWER SPECTRA

FIGURE A1.1

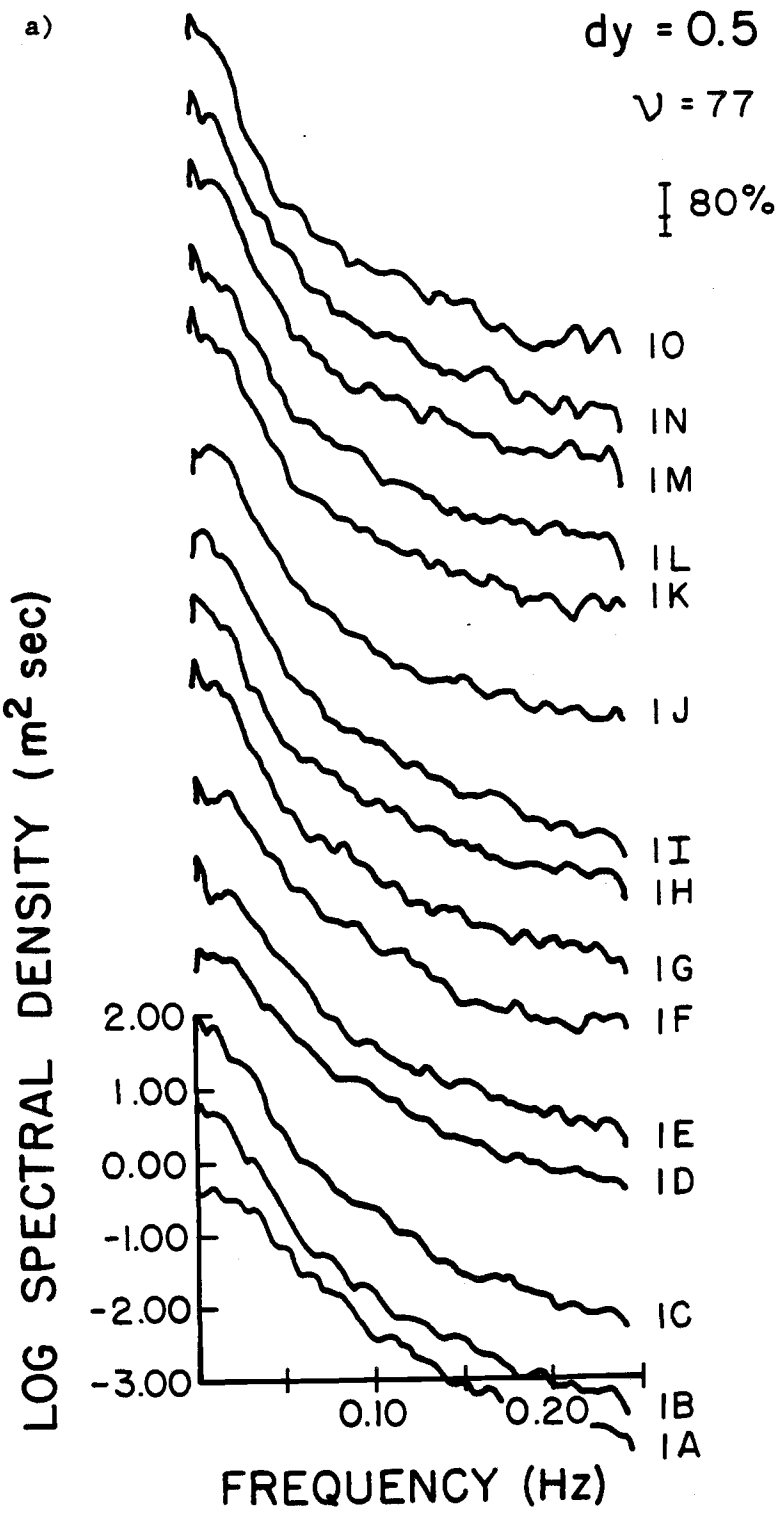

Figure A1.1. Spectra of runup for Days 1-4 (a-d) computed to the Nyquist frequency, stacked from south (bottom) to north (top). Labels correspond to transect labels in Figure 5.

b)

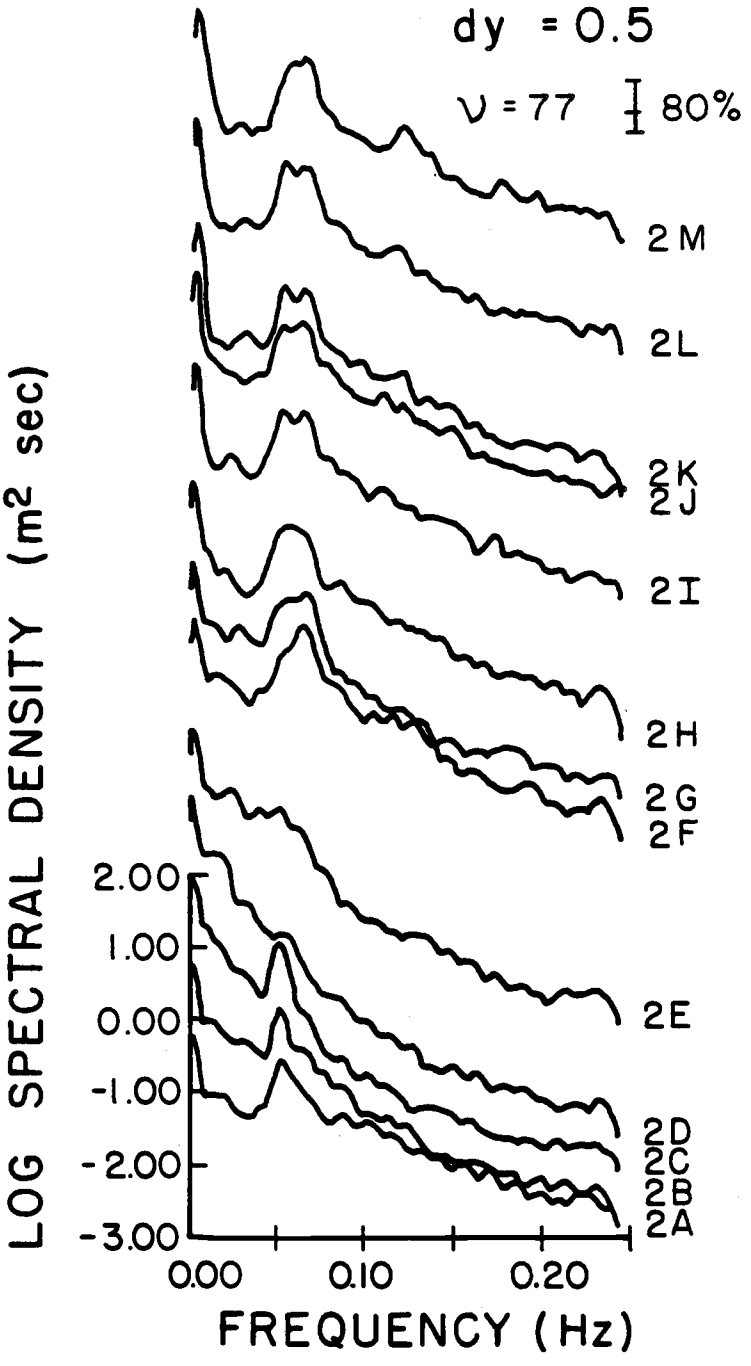

Figure A1.1 (continued).

c)

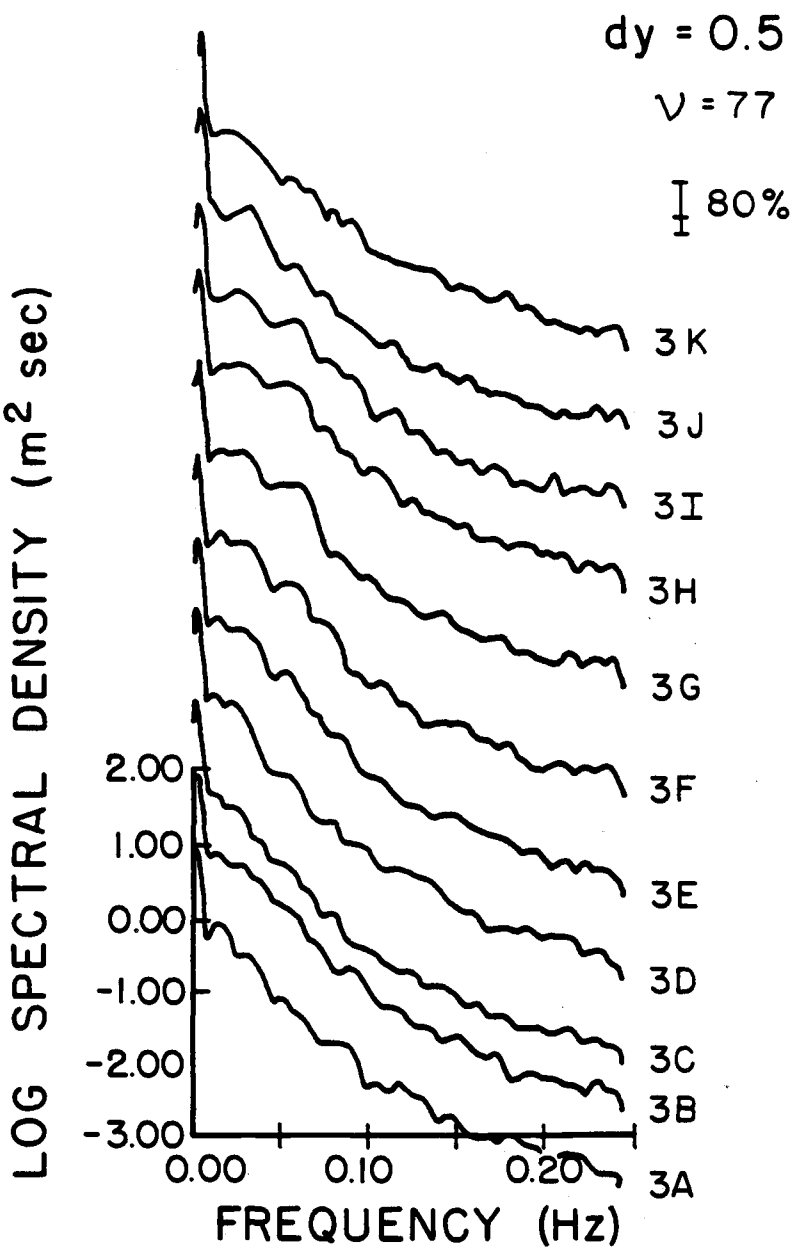

Figure A1.1 (continued).

d)

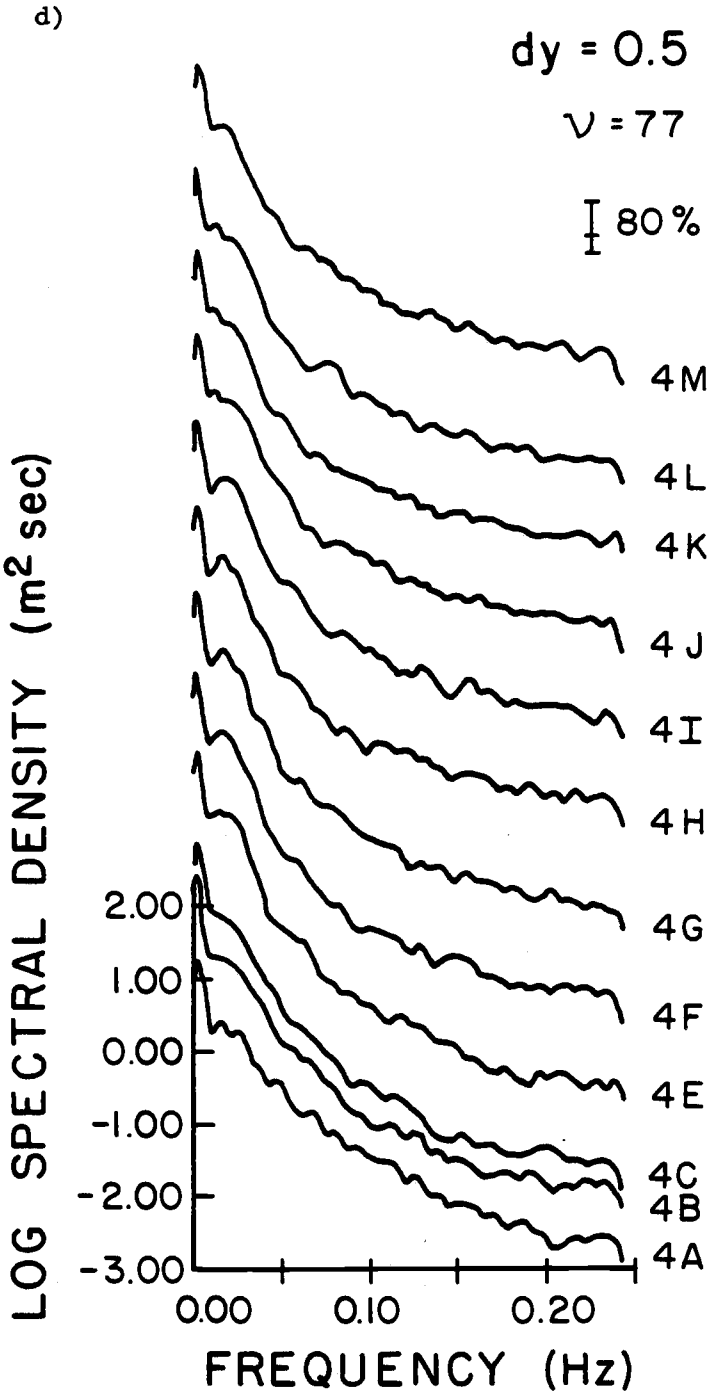

Figure A1.1 (continued).

APPENDIX 2:

LONGSHORE AMPLITUDE/PHASE PATTERNS OF COMPLEX EMPIRICAL ORTHOGONAL FUNCTION FACTORS OF WAVE RUNUP

FIGURES A2.1-A2.3

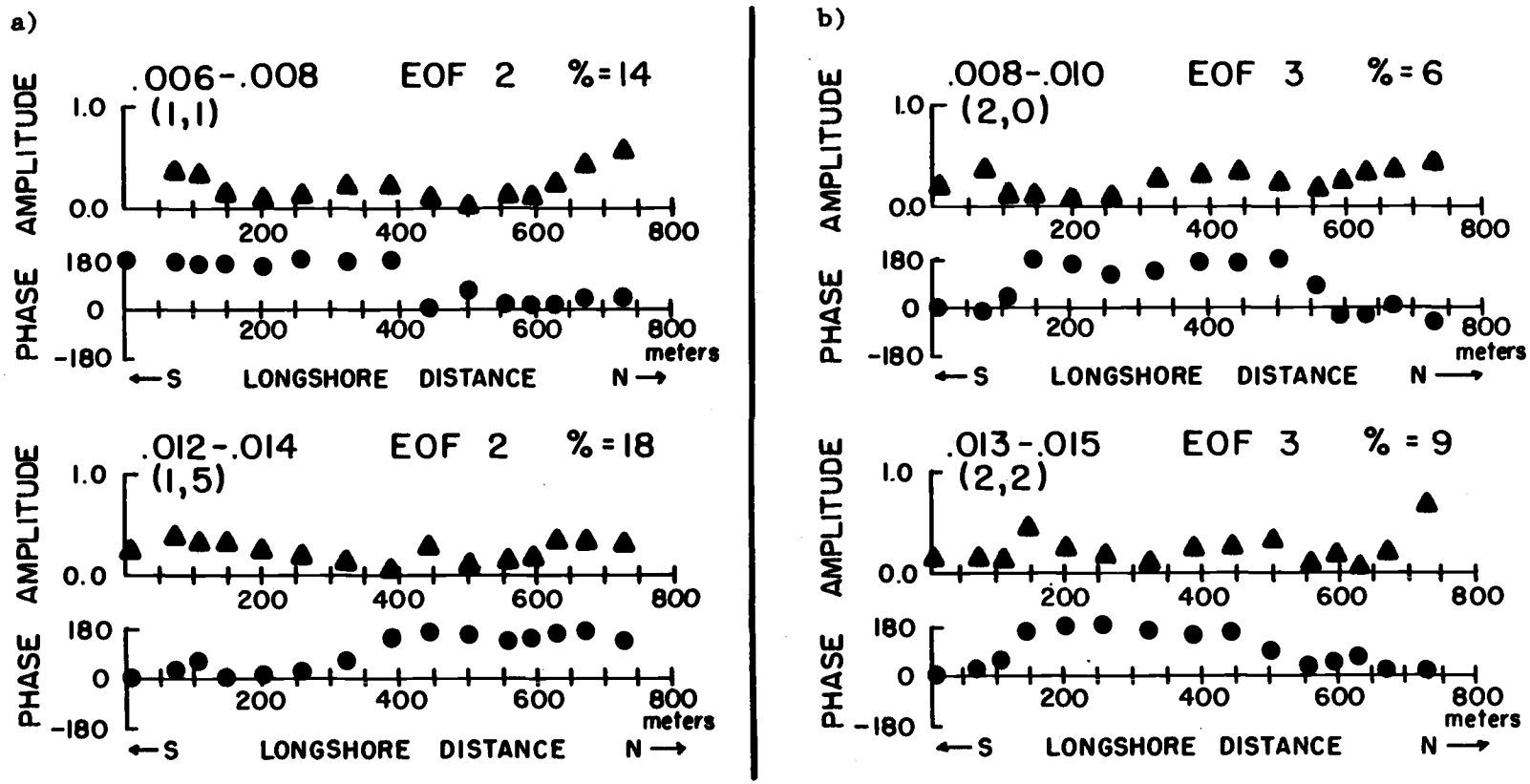

Figure A2.1. The amplitude/phase results from complex EOF decomposition of the longshore runup signal on Day 1, including the frequency band of each EOF and the percent of variance contributed to the band. (a) includes all EOF's that represent standing edge wave modes (m,n)=(1,n), and (b) includes modes (m,n)=(2,n).

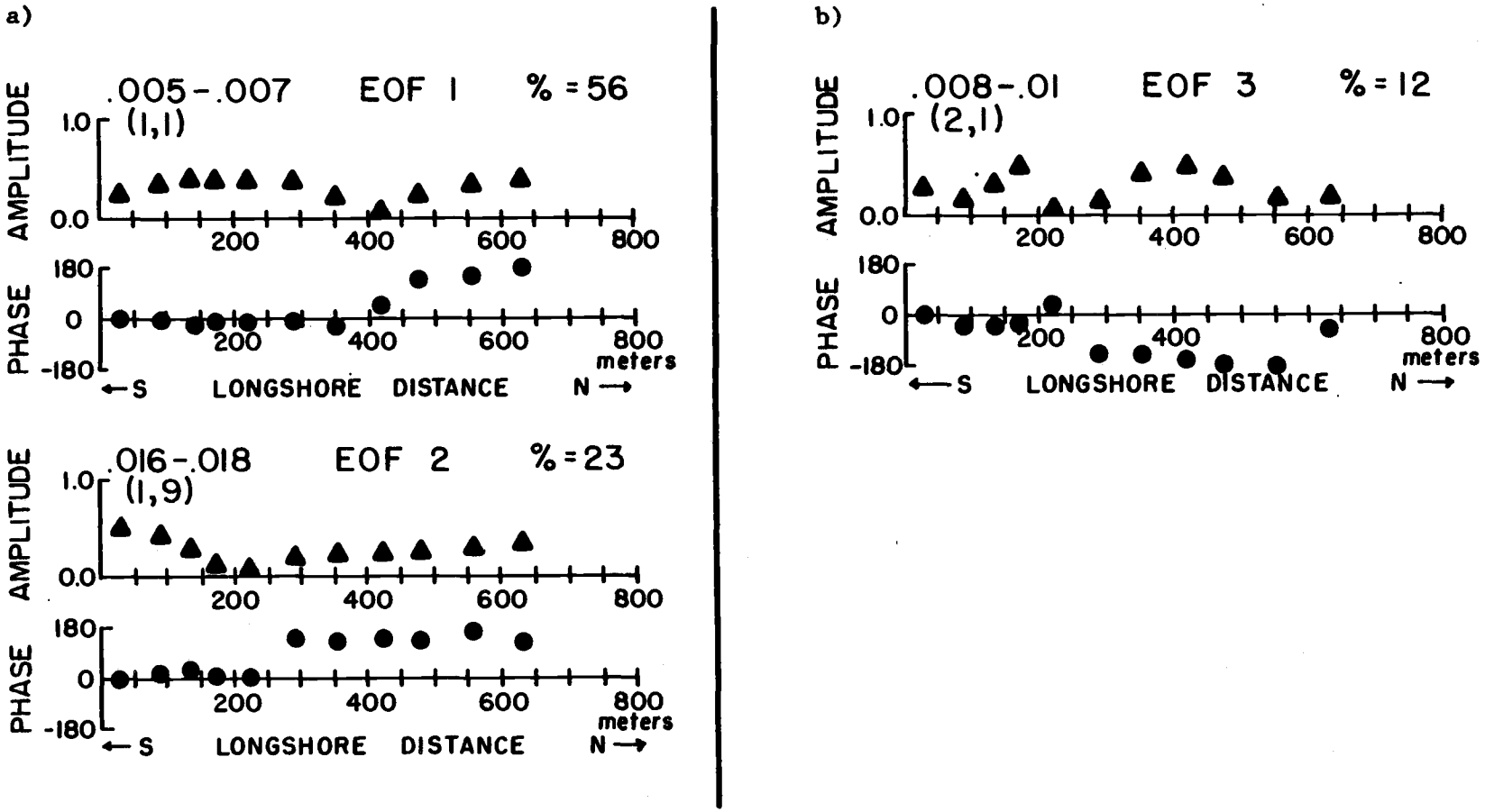

Figure A2.2. The amplitude/phase results from the complex EOF decomposition of the longshore runup signal on Day 3. See Figure A2.1 for a full explanation of the figure.

a)

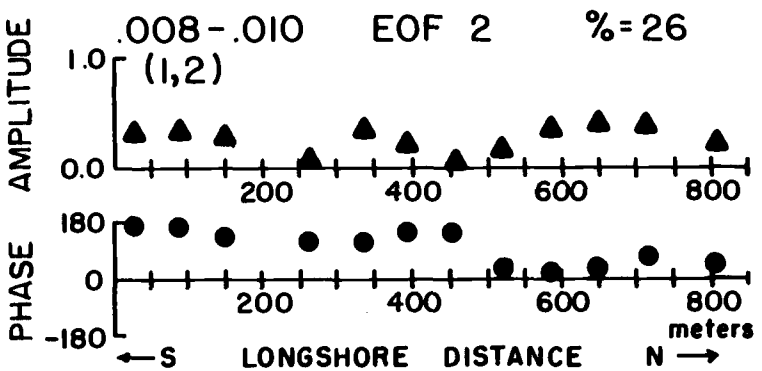

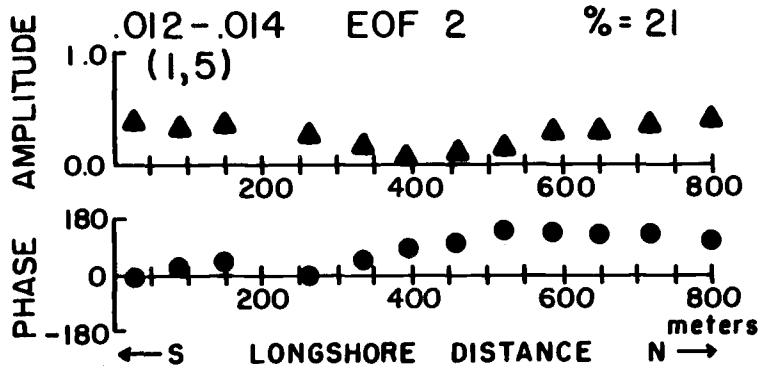

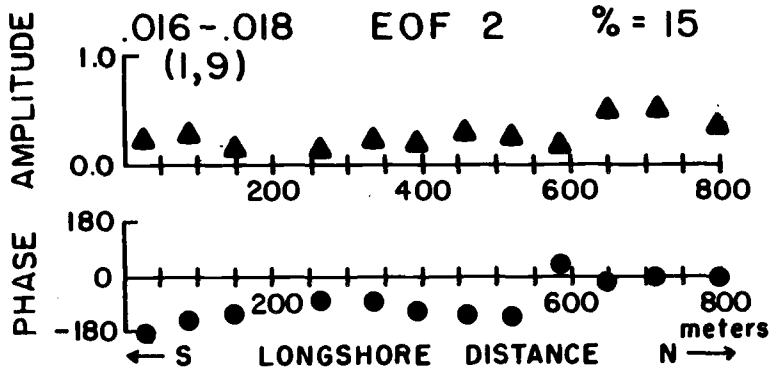

Figure A2.3. The amplitude/phase results from the complex EOF decomposition of the longshore runup signal on Day 4. See Figure A2.1 for a full explanation of the figure.

b)

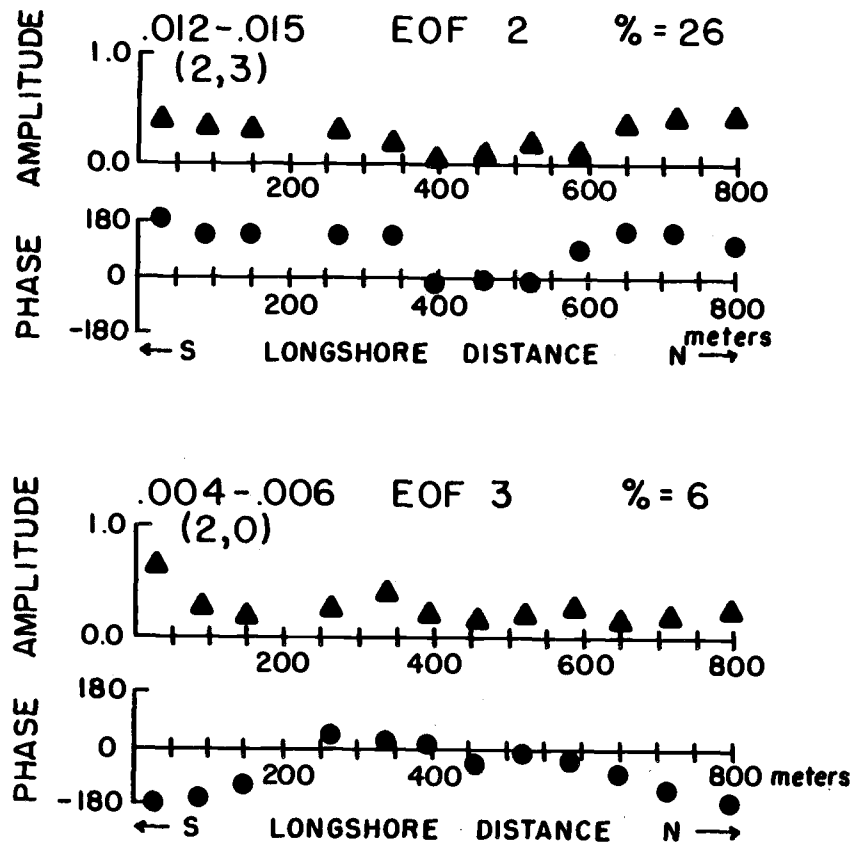

Figure A2.3 (continued).